



Microwave assisted facile fabrication of dual Z-scheme g-C₃N₄/ZnFe₂O₄/Bi₂S₃ photocatalyst for peroxymonosulphate mediated degradation of 2,4,6-Trichlorophenol: The mechanistic insights

Poulomi Sarkar, Sirshendu De, Sudarsan Neogi*

Department of Chemical Engineering, Indian Institute of Technology Kharagpur, Kharagpur 721302, India

ARTICLE INFO

Keywords:

Chlorophenols
Heterojunction composite
Dual Z-scheme
Catalytic degradation
Intermediate analysis

ABSTRACT

A ternary dual Z-scheme composite gCN/ZnFe₂O₄/Bi₂S₃ (ZFO/BS) was synthesized via a facile microwave assisted process and its photocatalytic potential was explored towards visible light driven removal of 2,4,6-trichlorophenol (TCP) with subsequent peroxymonosulfate (PMS) activation. Surface-bound Fe^{2+/3+} |_{surf}, Zn²⁺ |_{surf} and Bi^{3+/4+} |_{surf} were effective towards charge carrier channelization and evolution of reactive species. Highest catalytic activity was experienced for the catalyst with 10 wt% Bi₂S₃ (ZFO/BS(10)) and 98.9% TCP was removed with 0.25 gL⁻¹ catalyst and 1.0 gL⁻¹ PMS, under 60 mins visible light irradiation (intensity: 80 W). Construction of dual Z-scheme heterojunction was studied using XPS and the mechanism of e⁻/h⁺ separation was elucidated. In-depth radical scavenging and EPR analysis confirmed the coexistence and relative contributions of various reactive radicals towards degradation. Plausible TCP degradation pathway was designed based on intermediate analysis. This study elucidates the superiority of dual Z-scheme ternary heterojunction towards separation of photogenerated charge carriers and mineralization of various emerging contaminants.

1. Introduction

The imprudent use and disposal of toxic chemicals into the environment in the name of global industrialization is creating a massive ecological abolishment. Chlorophenols (CPs) are one of the most alarming halogenated aromatic compounds (HACs) which are generated as by-products of various industries and used directly as fungicides, pesticides, defoliant, preservatives of paint, glue, etc. 2,4,6-Trichlorophenol (TCP) is one of those intractable endocrine disrupting chemicals (EDCs) which has been marked as 'group B2' (potential carcinogenic precursor) by US Environment Protection Agency (EPA) [1]. Frequent existence of such refractory contaminant leads to bio-accumulation through the food chain which is detrimental for the global ecosystem. One of the emerging techniques widely investigated and employed successfully for degradation of such estranged organic pollutants is 'sulphate radical based advanced oxidation processes' (SR-AOPs) [2]. Unlike the conventional AOPs involving hydroxyl radicals (OH[•]), this technique employs sulphate radical (SO₄^{•-}) with higher redox potential (E⁰_{SO₄^{•-}/SO₄²⁻ = 2.5 – 3.1 V vs. NHE and E⁰_{OH[•]/OH⁻ =}}

1.7 – 2.6 V vs. NHE), elongated half-life (t_{1/2,SO₄^{•-} = 30 – 40 μs vs. t_{1/2,OH[•] ≈ 20 – 30 ns), effectiveness over wide pH range and higher selectivity towards unsaturated pollutants [2–4]. SO₄^{•-} radical is mostly evolved in the reaction medium through decomposition of either peroxymonosulphate (PMS) or peroxydisulphate (PDS). The peroxo bond (-O-O-) is situated symmetrically in the PDS molecule while in PMS, it is asymmetrically positioned. As result, for PMS, this bond can be easily cleaved. Moreover, decomposition of PMS generates HSO₅⁻ and SO₅²⁻ ions which react with organic molecules through e⁻-transfer, whereas, for the case of PDS, the generated S₂O₈²⁻ and SO₄²⁻ ions react with the contaminants via H-abstraction. The transition metal oxide photocatalyst mediated PMS activation has several advantages including higher reactivity due to lattice oxygen defects, redox interconversion and regeneration of surface metal ions, easy separability of the solid catalyst and resistance towards extreme operating conditions. Lately, growth of transition metal oxides onto graphitic carbon nitride (g-C₃N₄) manifested numerous advantages, including improved catalytic performance due to excellent electron (e⁻) transmission ability of the π-conjugated graphene-resembled structure, large surface area, synergic association of transition metals, and defect}}

* Corresponding author.

E-mail address: sneogi@che.iitkgp.ac.in (S. Neogi).

<https://doi.org/10.1016/j.apcatb.2022.121165>

Received 1 December 2021; Received in revised form 14 January 2022; Accepted 29 January 2022

Available online 2 February 2022

0926-3373/© 2022 Elsevier B.V. All rights reserved.

Nomenclature*Alphabetic symbols*

C	Residual TCP concentration at a specific time t (mg L^{-1})
C_0	Concentration of TCP in the feed solution (mg L^{-1})
E_{CB}	Conduction band energy
E_{VB}	Valence band energy
k_{obs}	Pseudo first order rate constant
A	Frequency factor
E_a	Activation energy

Abbreviation

AOP	Advanced Oxidation process
CB	Conduction band
CPs	Chlorophenols
CTC	Carbon tetrachloride
DCP	2,4-Dichlorophenol
EDC	Endocrine disrupting chemical
EDTA-2Na	Ethylenediaminetetraacetic acid disodium salt

g-C ₃ N ₄	Graphitic carbon nitride
HACs	halogenated aromatic compounds
His	L-Histidine
NOM	Natural organic matter
PBQ	para-Benzoquinone
PCP	4-Chlorophenol
PS	Persulphate
PDS	Peroxydisulphate
pH _{PZC}	pH at point of zero charge
TBA	Tertiary butyl alcohol
VB	Valance band
SR-AOP	Sulphate radical based advanced oxidation process
<i>surf</i>	Surface generated ions
TBA	Tertiary butyl alcohol
TCP	2,4,6-Trichlorophenol
TDS	Total dissolved solid
ROS	Reactive oxygen species
ZFO/BS	gCN/ZnFe ₂ O ₄ /Bi ₂ S ₃

rich framework with excellent physiochemical stability. ZnFe₂O₄ nanoparticles, apart from being a magnetic spinel compound, exhibited extensive applications in photocatalysis, solar cell, etc., due to its tuneable band gap (1.7–1.9 eV), better dispersibility, stability and non-toxicity towards aquatic life. Hybrid composites involving g-C₃N₄/ZnFe₂O₄ have already been synthesized by hydrothermal technique for photocatalytic degradation of various contaminants [5,6]. However, compared to conventional catalysts, a stable dual Z-scheme composite can exhibit superior catalytic potential by efficient e⁻/h⁺ partitioning and delocalisation of charge carriers on the catalytic active sites. This can be achieved by doping of metal sulphides (i.e., metal chalcogenides) into materials with C or defect-rich N co-doped C structure. Two-dimensional transition-metal based chalcogenide materials employ layered structure with abundant density of active sites and defect rich functional edges which can easily distribute the separated e⁻/h⁺ pairs, along with enhancing the light harvesting capability. Bismuth sulphide (Bi₂S₃) is a typical layered chalcogenide material having low-bandgap energy, hierarchically stacked layered two-dimensional structure and excellent visible-light harvesting property [7]. Recent researches indicated that the electromagnetic frequency of microwave (300 GHz to 300 MHz) can be a dynamic strategy to fabricate such functional nanocomposites [8]. The microwave energy can be transferred rapidly towards the dispersed or dissolved precursors in the medium and create instantaneous temperature hike (i.e., hot spots) to instigate the non-equilibrium reaction rate acceleration with high chemical yield and product purity. Moreover, compared to the hydrothermal and solvothermal methods, the microwave assisted synthesis is a less energy intensive and cost effective approach [9].

Herein, an innovative synthesis method is reported for fabrication of gCN/ZnFe₂O₄ composite, where g-C₃N₄ acts both as fuel and supporting matrix to generate magnetic ZnFe₂O₄ from its metal precursors [10]. Thereafter, microwave irradiation aided insitu growth and deposition of Bi₂S₃ flakes on the gCN/ZnFe₂O₄ was employed. The received microwave energy can instigate the electronic relaxation followed by the dipolar polarization, ionic conduction and prompt localized heating within the dissolved reactant molecules [8] to fabricate a novel gCN/ZnFe₂O₄/Bi₂S₃ ternary heterojunction composite. The synthesized material were characterized thoroughly using various techniques. The photocatalytic potential of the synthesized catalyst was evaluated through the visible light irradiation aided degradation of TCP aqueous solution, with PMS as oxidant. Influences of numerous process variables along with the ROS scavenger and mineralization efficiency were analysed in detail. The probable degradation pathways of TCP using

ZFO/BS/PMS system were also elucidated. Thus, the present study describes an implementable approach towards the efficient degeneration of various obnoxious contaminants in water, towards a cleaner environment.

2. Materials and experimental methods

All the chemicals utilized for the experiments belong to analytical grade and used as received, avoiding any further refinement. The deionized (DI) water (resistivity: 18.2MΩ.cm) used in the study was obtained from a Millipore water purifier supplied by M/s. Merck (India) Ltd. The detailed particulars of the required chemicals and the characterization instruments are summarized in section S1.

2.1. Synthesis procedure

The Graphitic carbon nitride (g-C₃N₄) and magnetic gCN/ZnFe₂O₄ composite were synthesized through a facile thermal polycondensation method [11] and an unique solid state mixing followed by oxidation-calcination step, respectively. The detailed synthesis processes for both these materials are described in section S2.

2.1.1. Synthesis of pure Bi₂S₃

Pure Bi₂S₃ nanoflakes were prepared with a microwave assisted synthesis process [12]. In an usual process, 4.2 g (8.66 mmol) of Bi(NO₃)₃·5 H₂O was added into 80 mL DI water. Then, 1.3 g (17.08 mmol) of Thiourea (CH₄N₂S) was added and a yellow suspension was immediately obtained. The mixture was stirred subsequently for 1 hr to reach complete homogenization. Then, the solution was taken in a sealed round bottom flask along-with the reflux system and placed in a microwave reactor (800 W, 2450 MHz). The reactor was programmed to reach at 180 °C with 25 °C min⁻¹ heating rate, thereafter maintaining constant temperature of 180 °C for 10 min and finally decreasing to ambient condition at a cooling rate of 25 °C min⁻¹. The microwave reactor generates a homogenous heating environment and thus diminish the thermal gradients and local heat pockets in the reaction solution under continuous magnetic stirring. This phenomenon is responsible for the effective nucleation and growth environment, leading uniform size distribution of the synthesized Bi₂S₃ nanoparticles [13]. The obtained precipitate was subjected to centrifugation and thorough washing with DI water and ethanol. The final pH of the wash solution was monitored till it attained neutral. The collected Bi₂S₃ powder was dried at 80 °C in a vacuum oven and used for characterization and experiments.

2.1.2. Synthesis of gCN/ ZnFe₂O₄/Bi₂S₃ composite

A facile microwave assisted synthesis method was adopted for insitu growth of Bi₂S₃ nanoflakes on the already prepared gCN/ZnFe₂O₄ composite. In an usual method, 4.2 g (8.66 mmol) of Bi(NO₃)₃·5 H₂O was added in 80 mL of DI water, under magnetic stirring. Next, 1.3 g (17.08 mmol) of Thiourea (CH₄N₂S) was mixed into the prior solution and the resultant yellowish suspension was stirred for another 1 hr. Pre-determined weight of gCN/ZnFe₂O₄ powder was mixed to the homogeneous solution and the resultant mixture was ultra-sonicated intermittently for 1 hr to obtain a uniform suspension. Next, the slurry was transferred into a round bottom flask with reflux arrangement into the microwave reactor. The reactor programming was kept same as mentioned before. After collecting and washing the as-synthesized black precipitate, it was dried at 80 °C and preserved for further experiments. During synthesis, the weight of gCN/ZnFe₂O₄ was varied suitably to attain specific Bi₂S₃ weight percentage in the final composite. The resultant composite (gCN/ZnFe₂O₄/Bi₂S₃) was levelled as ZFO/BS(x), where x indicates the doping content (in wt%) of Bi₂S₃ within the composite (e.g., x: 5, 10, 15, 20, etc.).

2.2. Kinetic study of photocatalytic oxidation

For the experimental analysis, 50 mL of 50 mgL⁻¹ TCP solution was taken in a flask (volume: 250 mL). Then, after adding specified weight of catalyst, the medium was continuously shaken (150 rpm) for 30 mins in dark to attain the adsorption-desorption equilibrium. Next, the degradation reaction was started by adding specified amount of oxidant (PMS/PDS) into the catalyst/TCP system and turning on the visible light ($\lambda > 420$ nm). The detailed protocols for experimentation and measurement of TCP concentration are mentioned in section S3.

2.3. Analytical methods

Details of various analytical methods, i.e., HPLC, LCMS/MS, TOC, used for the determination of residual CP concentration, identification of generated intermediates, and extent of mineralization, along with regeneration protocols, are specified in section S3.

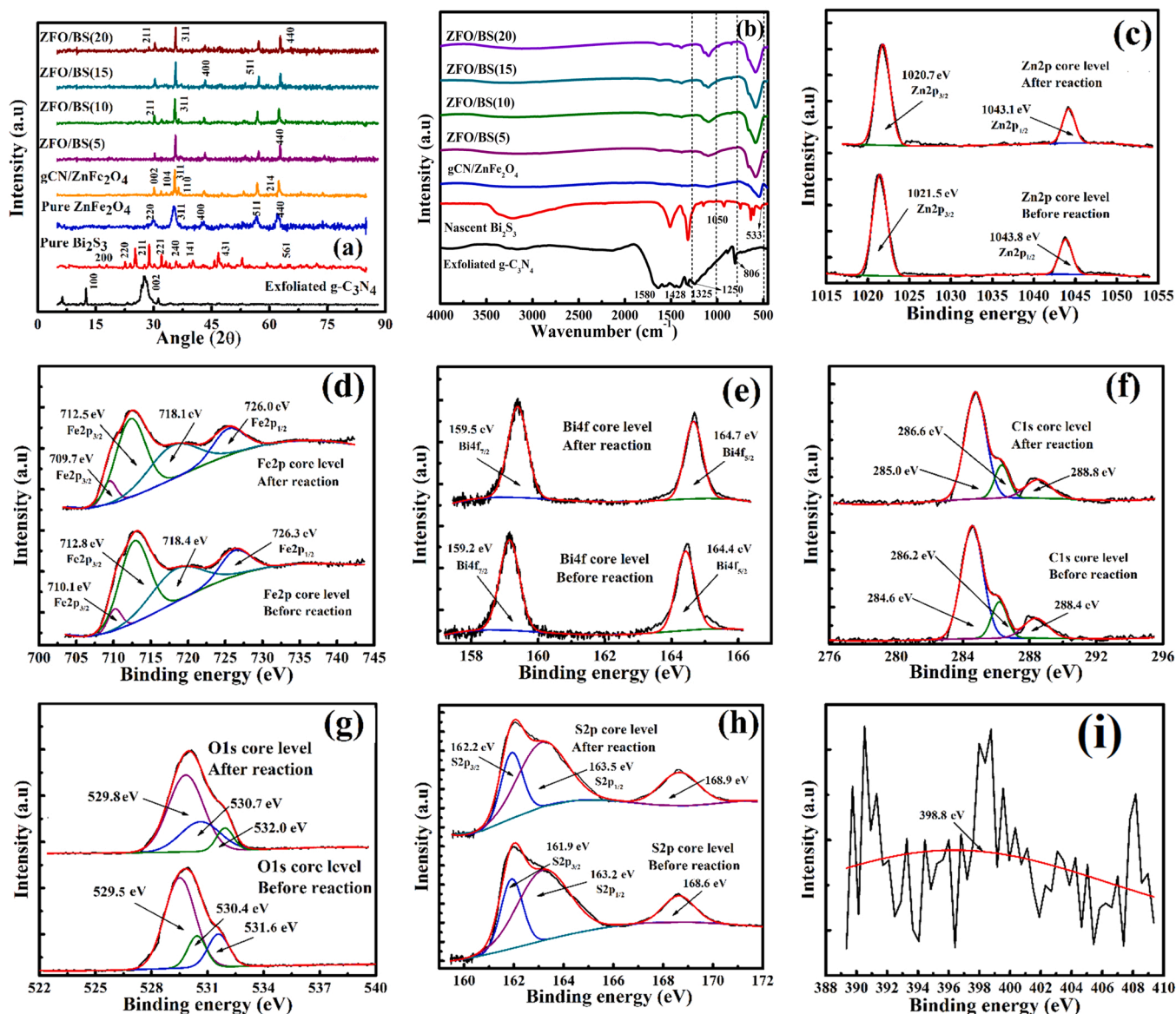


Fig. 1. XRD (a) and FTIR (b) spectra of bulk g-C₃N₄, nascent Bi₂S₃, ZnFe₂O₄, gCN/ZnFe₂O₄ composite, ZFO/BS(x) ternary composites; XPS analysis of (c) Zn 2p; (d) Fe 2p; (e) Bi 4f; (f) C 1s; (g) O 1s; (h) S 2p; (i) N 1s.

3. Results and discussion

3.1. Characterization of materials

3.1.1. Crystallography and surface functionalization

The XRD patterns of different primary components and resultant composites (gCN/ZnFe₂O₄ and ZFO/BS (x)) are depicted in Fig. 1a. For unmodified g-C₃N₄, the peak at 2θ: 12.51° and 27.3° represent the (100) in-planar arrangement of the tri-s-triazine units and inter planner stacking of graphitic units of carbon nitride (JCPDS no-87-1526) [6]. For pure ZnFe₂O₄, peaks are observed at 2θ: 30.31°, 35.69°, 43.37°, 53.57°, 57.25° and 62.85°, corresponding to (220), (311), (400), (422), (511) and (440) planes of cubic ZnFe₂O₄ with a spinel structure (JCPDS no-77-0011) [14]. The average crystalline size of ZnFe₂O₄ is determined as 19.6 nm, selecting the (311) plane's full width at half maximum (FWHM) using the Debye-Scherrer formula. For pristine Bi₂S₃, characteristic peaks are identified at 2θ: 13.11°, 20.79°, 28.75°, 32.81°, 35.79°, 42.15°, 47.97° and 69.19°, corresponding to (200), (220), (211), (221), (240), (141), (431) and (561) crystal planes, respectively (JCPDS no-17-0320) [7]. For the gCN/ZnFe₂O₄ binary composite, the peak for (002) plane of g-C₃N₄ is present, though that for the (100) plane disappeared completely owing to the misalignment of the periodic hierarchical arrangement of g-C₃N₄ (i.e., s-triazine units) during the combustion reaction. Similar characteristics can be observed for the ternary ZFO/BS(x) composites. It indicates that g-C₃N₄ acts as a sacrificial agent to provide a conductive carbon skeleton with abundant active sites through simultaneous loss of 'N' as N₂ gas during the synthesis of the composite. These carbon skeletons, composed of s-triazine units, with point defects of lost N atoms, are arranged in graphitic layered structure, which provides strong support for growth of other layered materials as well as a conductive platform for photogenerated charge carriers. These defective carbon layers are held together by Vander walls forces and possess high mechanical and thermal stability. After the incorporation of Bi₂S₃ in gCN/ZnFe₂O₄, characteristic peaks of each component are identified. For example, 20 wt% Bi₂S₃ doped gCN/ZnFe₂O₄ (ZFO/BS(20)) exhibits prominent peaks at 2θ: 27.53°, 28.62° and 35.53°, owing to the (002) plane of g-C₃N₄, (211) plane of Bi₂S₃ and (311) plane of ZnFe₂O₄, respectively. The other peaks at 2θ: 47.85° and 53.45° are generated from (431) and (422) planes of Bi₂S₃ and ZnFe₂O₄, respectively. Moreover, with increase of Bi₂S₃ content in the composites, the peak at 28.62° became more prominent, characteristic of (211) plane of Bi₂S₃. Thus, the XRD analysis infers the successful synthesis of the ternary heterojunction and no variation of the overall crystalline arrangement of the spinel ZnFe₂O₄, due to the incorporation of graphitic C-layer and insitu growth of Bi₂S₃.

The preparation of binary gCN/ZnFe₂O₄ composite involves aqueous phase mixing of ZnSO₄, 7 H₂O and Fe₂(SO₄)₃, H₂O and subsequent drying which generate a homogeneous salt mixture. Addition of NaCl (mole ratio of 1:8) in this mixture and further calcination at high temperature (550 °C) in open atmosphere generate NaFe(SO₄)₂ and Na₃Fe(SO₄)₃ which are subsequently transformed into β-Fe₂O₃ [15]. This phase of Fe₂O₃ is metastable and transient under thermal treatment. As a result, this transient β-Fe₂O₃ is transformed into stable α-Fe₂O₃ with rhombohedral structure which imparts magnetic property in the spinel ZnFe₂O₄. Moreover, this topotactic phase transformation is dependent on several factors, like, particle size, overall surface area and/or presence of impurities/external agents [16]. Therefore, the addition of g-C₃N₄ in the system may impose favourable effects towards this transformation and generates N-less defective framework. The XRD spectrum establishes that the gCN/ZnFe₂O₄ composite contains small amount of α-Fe₂O₃ phase along with the spinel ZnFe₂O₄ structure. Specifically, the small peaks at 2θ: 33.2°, 35.6°, 40.9° and 62.3° are indexed to the (104), (110), (113) and (214) planes of rhombohedral α-Fe₂O₃ phase, having a corundum structure with hexagonal close packed O sublattice and two-thirds of the octahedral sites filled with Fe ions (JCPDS card no: 33-0664). [17]. Moreover, the chloride-salt

directed one-step calcination route helps to generate defects within the g-C₃N₄ structure. The presence of chloride salt is also capable to form well-ordered, highly crystalline products with improved micro and mesoporosity through solvation effects to enhance the nucleation and mass transfer rates [18].

FTIR spectra of individual components (nascent g-C₃N₄, nascent Bi₂S₃) and composite catalysts (gCN/ZnFe₂O₄, ZFO/BS(x)) are depicted in Fig. 1b. For nascent g-C₃N₄, the wide band in the region 3000–3600 cm⁻¹ is generated due to the stretching of O-H bonds, from adsorbed H₂O [19]. Also, characteristic bands in the range of 900–1800 cm⁻¹, with peaks at 1250 cm⁻¹, 1325 cm⁻¹, 1428 cm⁻¹, 1580 cm⁻¹ and 1640 cm⁻¹ are assigned to both the trigonal C-N(C)-N-C (full condensation) and connective C-NH-C units [20]. Breathing vibration of the S-triazine ring generates another peak at 806 cm⁻¹. For pure Bi₂S₃, two weak peaks are generated at 1050 cm⁻¹ and 2127 cm⁻¹, characteristic of the in-plane ring vibration. Another small yet sharp peak at 533 cm⁻¹ denotes the Bi-S bond vibration [21,22]. For nascent gCN/ZnFe₂O₄, two peaks at 418 cm⁻¹ and 571 cm⁻¹ denote the symmetric stretching vibration of Zn-O and Fe-O bonds, respectively [23]. A less prominent peak at 1637 cm⁻¹ indicates the O-H stretching vibration. ZFO/BS composites contain the major peaks of all the individual constituents. In particular, the peaks at 415 cm⁻¹, 535 cm⁻¹, 575 cm⁻¹ are indicative towards the Zn-O, Bi-S and Fe-O bond vibrations. For any of the ZFO/BS composites, no peak in the 800–810 cm⁻¹ range indicates the absence of s-triazine unit of g-C₃N₄ in the framework. This result indicates the absence of any graphitic N in the material and its loss as N₂ gas during the combustion synthesis step. Some weak peaks in the 1300–1650 cm⁻¹ region are evolved from in-plane ring vibration of graphitic carbon layers and Bi₂S₃ structure. Moreover, with gradual doping of Bi₂S₃ in the composite, the peak due to the Bi-S bond becomes sharp and intense. Thus, this analysis depicts a favourable confirmation of successful formation of the composite and possible chemical and electronic interactions among the individual components.

High-resolution XPS spectra of the ternary composite (both nascent and reacted) are presented in Fig. 1(c-i). For pristine ZFO/BS composite, the Zn2p (Fig. 1c) spectrum produces two major peaks at 1021.5 eV (Zn2p_{3/2}) and 1043.8 eV (Zn2p_{1/2}), for Zn²⁺_{surf} in spinel ZnFe₂O₄. In the Fe2p spectrum (Fig. 1d), four peaks are identified at 710.1 eV (Fe2p_{3/2}, Fe²⁺ in tetrahedral sites), 712.8 eV (Fe2p_{3/2}, Fe³⁺ in octahedral sites), 718.4 eV (sat.) and 726.3 eV (Fe2p_{1/2}, Fe³⁺), indicating dominance of Fe³⁺_{surf} on catalyst surface, with minor content of Fe²⁺_{surf}. Moreover, deconvolution of the Bi4f spectrum exhibits peaks at 159.2 eV (Bi4f_{7/2}) and 164.4 eV (Bi4f_{5/2}), respectively, due to Bi³⁺_{surf} (Fig. 1e). The spin orbit splitting of 5.2 eV further strengthens the existence of Bi³⁺_{surf}. The C1s spectrum (Fig. 1f) is fitted into three peaks at 284.6 eV, 286.2 eV and 288.4 eV which can be indexed as C=C/C-C, C=O and N-C≡N in g-C₃N₄, respectively. Three peaks are observed in the O1s spectra of nascent composite at 529.5 eV, 530.4 eV and 531.6 eV, due to surface lattice oxygen (M-O, M: Zn, Fe), metal-hydroxyl and carbon-hydroxyl groups (M-OH and C-OH, M: Zn, Fe) and surface adsorbed oxygen (O_{ads}, from adsorbed H₂O), respectively (Fig. 1g). The S2p spectrum generates two peaks at 161.9 eV (S2p_{3/2}), 163.2 eV (S2p_{1/2}) and 168.6 eV (sat.) (Fig. 1h). After photocatalytic reaction, the Zn2p peaks are shifted to 1020.7 eV and 1043.1 eV (compared to 1021.5 eV and 1043.8 eV for pristine Zn2p), respectively. Similarly, in the reacted catalyst, the corresponding Fe2p peaks shift at 709.7 eV (pristine: 710.1 eV), 712.5 eV (pristine: 712.8 eV) and 726.0 eV (pristine: 726.3 eV), respectively. These results indicate that Zn²⁺_{surf} and Fe³⁺_{surf} were partially reduced to Zn⁺_{surf} and Fe²⁺_{surf} during the photocatalytic reaction. So, e⁻s have been transferred towards the ZnFe₂O₄ framework, mainly from the adsorbed PMS species and ionized TCP molecules along with the conductive gCN framework. On the other hand, the peaks of C1s spectrum of the reacted catalyst are minutely shifted to 285.0 eV, 286.6 eV and 288.8 eV, compared to the pristine catalyst with peaks at 284.6 eV,

286.2 eV and 288.4 eV, indicating the release of e^- s from g-C₃N₄ framework during the reaction. Finally, for Bi4f spectrum, the peaks are slightly shifted to higher energies in the reacted composite (nascent: 159.2 eV, 164.4 eV and reacted: 159.5 eV, 164.7 eV), implying loss of e^- s and partial oxidation of the $\text{Bi}^{3+}_{\text{surf.}}$ to $\text{Bi}^{4+}_{\text{surf.}}$. For the case of O1s spectrum in reacted catalyst, the shifting of peaks to slightly higher binding energies (i.e., 529.8 eV, 530.7 eV and 532.0 eV), along with increase of peak area of the M-OH group imply that during reaction, inner-sphere metal-hydroxyl intermediates are generated on the catalyst surface and e^- s have been accepted by the lattice and surface adsorbed O atoms. In the reacted catalyst, the S2p peaks are slightly shifted to 162.2 eV (S2p_{3/2}) and 163.5 eV (S2p_{1/2}), respectively, compared to the pristine composite (161.9 eV for S2p_{3/2} and 163.2 eV for S2p_{1/2}), implying transfer of e^- s during the photocatalytic reaction. A very weak peak for N1s is identified both for nascent and reacted catalysts at 398.8 eV, which may be due to the minor C=N – C bonding on the surface (Fig. 1i). This very small peak can be ascribed to the negligible presence of 'N' atom on the surface and within few atomic layers of the graphitic framework. Most of the constituent 'N' atoms have been lost as N₂ gas, during the insitu solid combustion process, as also evidenced from the XRD and FTIR analysis.

3.1.2. Morphological and microstructural analysis

The overall morphology and crystal structure of primary components, binary and ternary heterojunctions are examined using FESEM analysis and the microscopic images are illustrated in Fig. 2(a-f).

Pure g-C₃N₄ has a two-dimensional lamellar structure (Fig. 2a), with uniform porous surface morphology. Structure of Bi₂S₃ appeared as hierarchical, stacked interlayers with flake-like morphology, arranged in regular patterns (Fig. 2b). Pure ZnFe₂O₄ and insitu grown ZnFe₂O₄ nanoparticles on the porous g-C₃N₄ are found to be crystalline and consisted of agglomerated spherical particles with average size of 20 nm (Fig. 2(c,d)), due to the strong magnetic interaction and high surface area owing to their nanoscale size. Incorporation of Bi₂S₃ onto the gCN/ZnFe₂O₄ composite creates a hybrid surface morphology, similar to the crystal structure of individual components (Fig. 2(e,f)). The presence of Bi₂S₃ flakes on the composite particles is evident from both the figures, along with the increasing density of deposited particles with the increase in wt% of Bi₂S₃ in the ternary composite. This kind of evenly dispersed structure of the composite is quite beneficial for harvesting of incident irradiation and effective separation of photo generated e^-/h^+ pairs [6].

The ternary ZFO/BS(10) composite is also investigated using HRTEM analysis and the corresponding images are presented in Fig. 2(g-k). From Fig. 2(g,h), distinct gCN/ZnFe₂O₄ particles, with surface-grown Bi₂S₃ sheets can be clearly identified. Similar to the FESEM images, the particles are observed as agglomerated due to the high magnetic moment. The HRTEM images (Fig. 2(i,j)) represent the well-defined interfacial heterojunction between the insitu grown Bi₂S₃ sheets on gCN/ZnFe₂O₄ framework. The mesh-like distributed sheet represents graphitic layers with d -spacing of 0.254 nm, corresponding to the (002) plane of g-C₃N₄. Above the g-C₃N₄ sheets, the dark and continuous layer with d -spacings of 0.32 nm is the (311) plane of the spinel ZnFe₂O₄ nanoparticles. Coexisting with both these components, an inscribed dark region can be identified (Fig. 2h) as embedded Bi₂S₃ with d -spacing of 0.39 nm, corresponding to the (220) plane of Bi₂S₃. Interestingly, all the three components of ZFO/BS coexist with intimate and continuous boundaries to establish a proper interfacial heterojunction which is highly beneficial for charge carrier migration and distribution. The corresponding SAED pattern (Fig. 2k) shows three distinct concentric rings, corresponding to the (002) plane of g-C₃N₄, (311) plane of ZnFe₂O₄ and (220) plane of Bi₂S₃, respectively. Also, no concentric ring is identified corresponding to the (100) plane of g-C₃N₄ which indicates loss of N atoms and formation of a defective graphitic carbon network, resulting non-existent s-triazine ring structure. The corresponding EDS image of the ternary composite (Fig. 2l) indicates the absence of 'N' atom due to the loss as N₂ gas during the solid-state combustion of the synthesis process, as already

been indicated in XRD, FTIR and XPS analysis.

3.1.3. The optical, textural, magnetic and surface charge analysis

The UV-Vis DRS analysis determines the optical properties of the materials and the corresponding band gap energies (E_g), which aid in the interpretation of the light harvesting capacity of the heterojunction composite. The optical property of thermally exfoliated g-C₃N₄, nascent Bi₂S₃, nascent gCN/ZnFe₂O₄ and pristine ZFO/BS(10) are investigated and the results along with the calculation details are presented in Fig. 3 (a,b). The E_g of exfoliated g-C₃N₄ is obtained as 2.84 eV [24]. The synthesized pure Bi₂S₃ is intrinsically black in colour with broad absorption from 200 nm to 800 nm, with a small E_g of 1.38 eV. The E_g of nascent ZnFe₂O₄ is 1.78 eV [25], manifested to efficient spin-allowed $d-d$ charge transfer and ligand to metal charge shifting from the O atoms to the Fe³⁺ sites. Hence, incorporation of Bi₂S₃ onto gCN/ZnFe₂O₄ composite favours red shift of absorption band and utilizing more visible range irradiation. The maximum absorbance of ZFO/BS(10) is experienced at 560 nm. Also, exfoliated g-C₃N₄ displays absorption in the 200–450 nm range, which signifies charge shifting from the valence band (VB) of the N2p orbitals towards the conduction band (CB) of C2p.

To realize the charge transfer efficacy of the individual single components (i.e., nascent g-C₃N₄, ZnFe₂O₄ and Bi₂S₃), binary composites (i.e., gCN/ZnFe₂O₄, ZnFe₂O₄/Bi₂S₃, gCN/Bi₂S₃) and ternary composite (ZFO/BS(10)), photoluminescence (PL) spectroscopic analysis is conducted and the corresponding results are presented in Fig. 3c. The PL intensity of ZFO/BS(10) is the weakest among all the materials which implies that most efficient charge separation is obtained due to the possible formation of dual Z-scheme alignment. On the other hand, the binary composites generate slightly stronger PL intensities, implying the formation of binary heterojunction to be less effective than ternary configuration towards charge separation and increasing their effective lifetime. Moreover, among the three binary composites, gCN/Bi₂S₃ shows minimum PL intensity, compared to gCN/ZnFe₂O₄ and ZnFe₂O₄/Bi₂S₃, due to most effective separation of e^-/h^+ pairs at the farthest possible points for the binary composites. Lastly, the primary components show strong PL intensities due to faster charge recombination and reduced effective lifetime of photogenerated charge carriers.

The parameters for pore structure and surface area for the fabricated g-C₃N₄, Bi₂S₃, gCN/ZnFe₂O₄ and ZFO/BS(10) ternary composite are analysed using the Brunauer-Emmett-Teller (BET) analysis. The generated N₂ adsorption-desorption isotherms, along with the BJH pore size distribution curves are presented in Figs. S1(a,b). All the adsorption-desorption isotherms can be classified as type-IV curves with the relative pressure (P/P_0) varying in the range of 0.01–1.0. The isotherm of pure g-C₃N₄ exhibits H3 hysteresis curve, implying the mesoporous nature of the material with slit-shaped pores whereas pure Bi₂S₃ exhibits type-IV isotherm with H4 hysteresis, indicating the existence of narrow slit pores. Both the binary (gCN/ZnFe₂O₄) and ternary (ZFO/BS(10)) composites exhibit the type-IV H3 hysteresis curve with higher volume of adsorption and higher specific surface area (10.6 m²g⁻¹ for ZFO/BS(10)). Though the specific surface area has been decreased slightly than pure g-C₃N₄ (S_{BET} : 13.0 m²g⁻¹) after composite formation, still it is substantially higher than the pure Bi₂S₃ (S_{BET} : 3.7 m²g⁻¹) and the gCN/ZnFe₂O₄ binary composite (S_{BET} : 6.2 m²g⁻¹). The corresponding pore size distribution analysis (Fig. S1b) indicates that all the pores in the components are mainly distributed in the size range of 10–50 nm. Pure g-C₃N₄ exhibits a broader pore distribution with the peak centred at 24 nm, whereas for ZFO/BS(10), comparatively narrow pore size distribution, with the maximum pore size peak at 18 nm suggests the existence of mesoporous structure. Thus, it can be interpreted that g-C₃N₄ is the ideal support matrix for the insitu growth and deposition of ZnFe₂O₄ and Bi₂S₃. The superior porous structure of the (ZFO/BS(10)) composite induces better adsorptivity and provides larger exposure towards the surface generated ROS which aid in efficient photocatalytic degradation of the targeted TCP molecules.

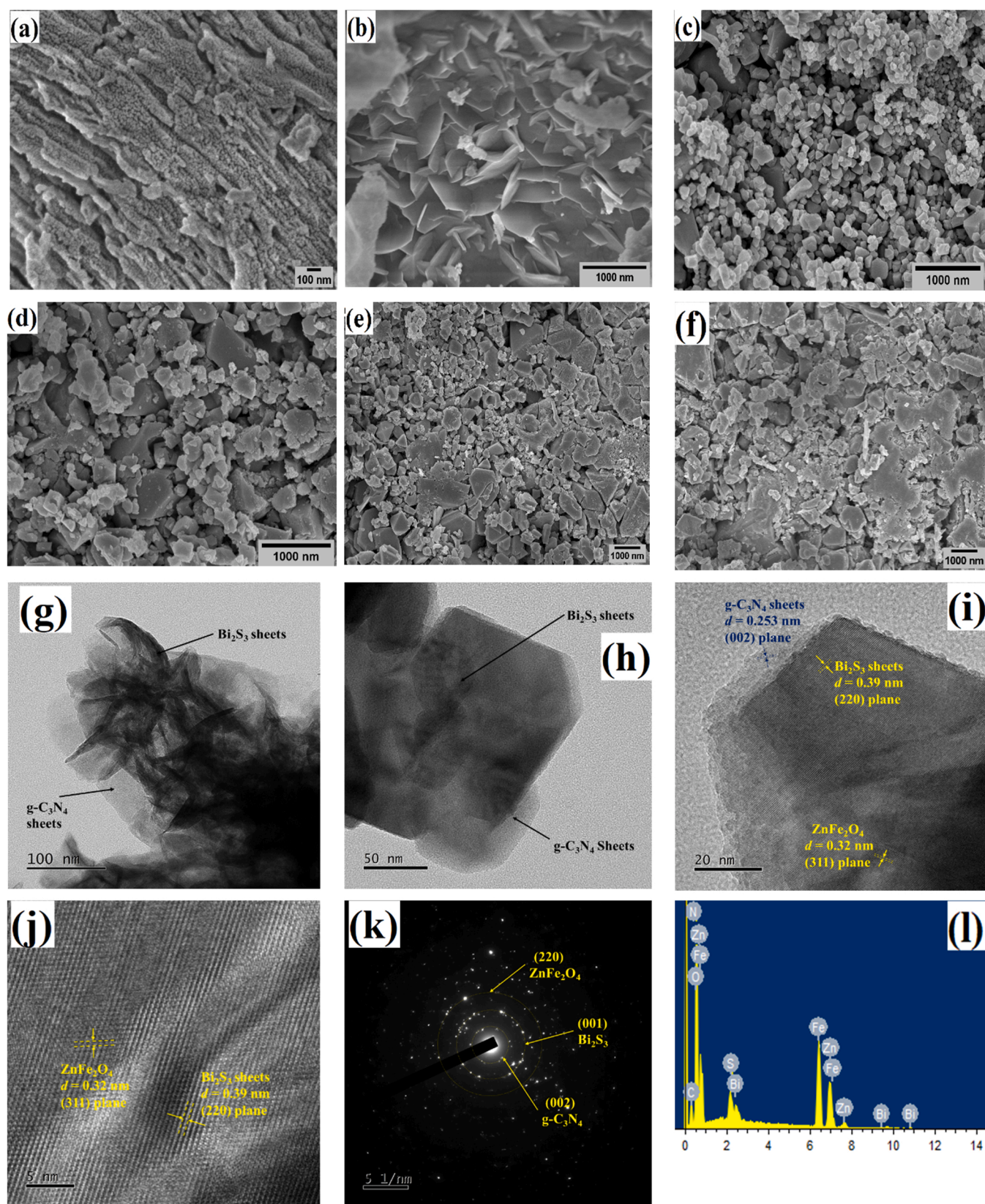


Fig. 2. SEM images of (a) exfoliated g-C₃N₄; (b) pristine Bi₂S₃; (c) ZnFe₂O₄; (d) gCN/ ZnFe₂O₄; (e) ZFO/BS(5); (f) ZFO/BS(10); (g,h) STEM images; (i,j) HRTEM analysis; (k) SAED patterns; (l) EDS analysis of ZFO/BS(10).

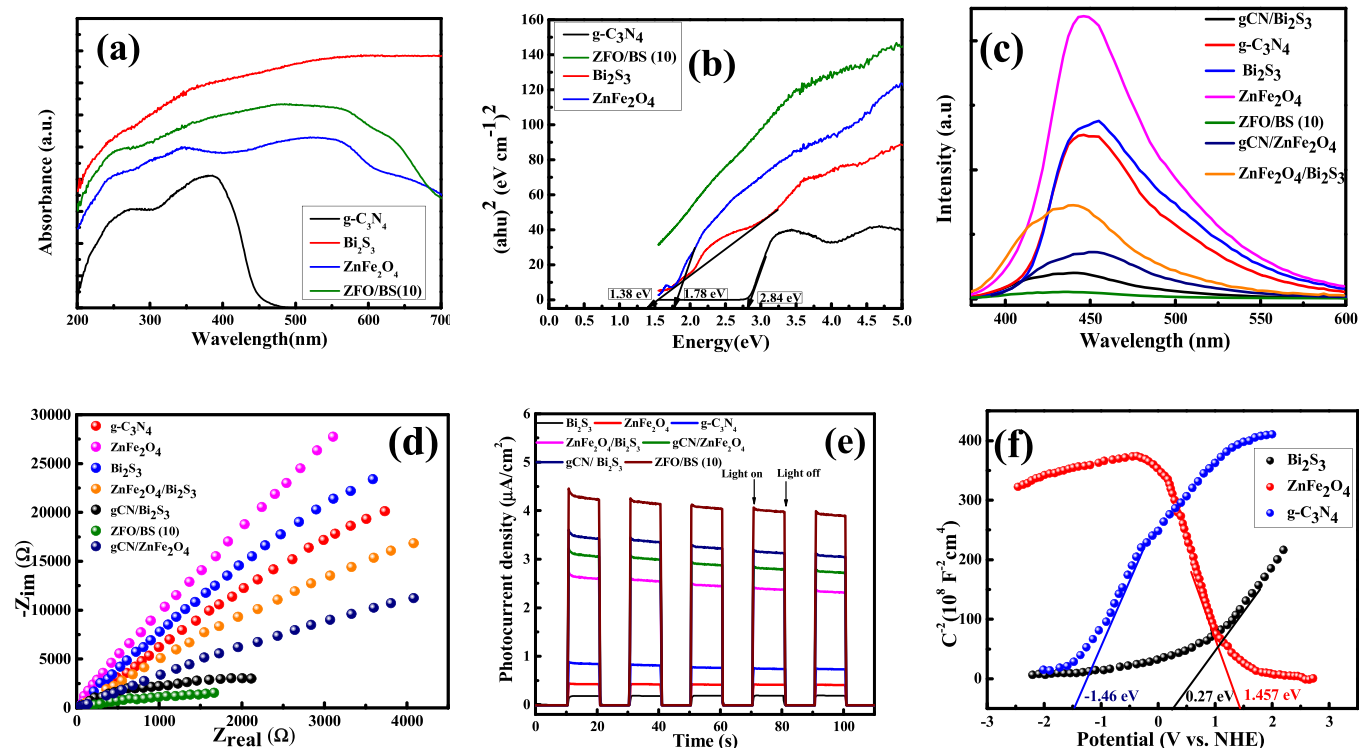


Fig. 3. (a) DRS spectra; (b) Tauc's plot; (c) PL spectra; (d) EIS plots; (e) Photocurrent response; (f) Mott-Schottky analysis plots for g-C₃N₄, ZnFe₂O₄, Bi₂S₃, binary and ternary composites.

The magnetic property of the materials are analysed using SQUID-VSM and the corresponding hysteresis plot is illustrated in Fig. S2a. The magnitude of saturation magnetization (M_s) of gCN/ZnFe₂O₄ (12.47 emu/g) is almost double to that of ZFO/BS(10) (6.16 emu/g). Doping of non-magnetic Bi₂S₃ into the composite might have led to a slight decrease in saturation magnetization value. However, the composite still possesses sufficiently strong magnetic moment to impart high separability from the solution using an applied magnetic field, which increases its applicability in actual process applications and regeneration.

Alteration of zeta potential of ZFO/BS(10) with solution pH is presented in Fig. S2b, which shows that the composite has an isoelectric point (i.e., point of zero charge, pH_{pzc}) of 5. So, above (below) the pH_{pzc} , the catalyst particle is negatively (positively) charged owing to its preferential capture of H⁺ or OH⁻ ions, depending on the solution pH. Also, the dissociation of sulphide groups on the surface of the catalyst (i.e., exposed edges of Bi₂S₃ flakes) plays significant roles in attainment of surface charge. Hydrolysis of S-atoms of the Bi₂S₃ particles imparts characteristic surface charge of the overall compound, due to adsorption of H⁺ or OH⁻ ions. Moreover, the surface charge of the ZFO/BS(10) catalyst varies within 43 mV (pH: 2) to -50 mV (pH: 12).

3.1.4. Photoelectrochemical analysis

To determine the photo-responsiveness and charge carrier separation efficiency of the individual single components (i.e., nascent g-C₃N₄, ZnFe₂O₄ and Bi₂S₃), binary composites (i.e., gCN/ZnFe₂O₄, ZnFe₂O₄/Bi₂S₃, gCN/Bi₂S₃) and ternary composite (ZFO/BS), electron impedance spectroscopy (EIS) and photocurrent response analysis are measured. The generated Nyquist plots and photocurrent responses are depicted in Fig. 3(d,e). For the ternary composite (ZFO/BS), the arc radius is smallest in the low frequency region which implies the strongest resistance against charge carrier recombination. On the other hand, for each of the binary composites, the arc radius is smaller than corresponding single components. This result implies that the formation of heterojunction (either binary or ternary) is beneficial towards systematized

charge separation and increase the resistance towards recombination of photogenerated charge carriers. Further, among the binary composites, gCN/Bi₂S₃ attains the maximum charge separation capability, compared to both gCN/ZnFe₂O₄ and ZnFe₂O₄/Bi₂S₃.

For the photocurrent response, the ternary composite (ZFO/BS(10)) shows the strongest response in the light irradiation cycle. The binary composites generate slightly weaker response than ZFO/BS(10) but it is 3.5–19.8 times stronger compared to the responses of the nascent single components. It can be observed that introduction of Bi₂S₃ in the composite greatly improves their photo-responsiveness (due to quantum confinement effect and local *d-d* transitions) which is directly corroborative with the UV-Vis DRS analysis. Similar trend is also observed among the various binary composites, where gCN/Bi₂S₃ generates stronger peak of photocurrent than the other composites, i.e., gCN/ZnFe₂O₄ and ZnFe₂O₄/Bi₂S₃.

The Mott-Schottky analysis of the nascent single components (i.e., g-C₃N₄, ZnFe₂O₄ and Bi₂S₃) are shown in Fig. 3f. The flat-band potential (E_{fb}) of any materials can be obtained from the linear interpolation of the $1/C^2$ curve with the potential (E) axis. The relationships between $1/C^2$ and E are given as (for *n* and *p* type semiconductors):

$$\text{For } n\text{-type semiconductors: } \frac{1}{C^2} = \frac{2}{e\epsilon_r\epsilon_0 N_D} \left(E - E_{fb} - \frac{k_B T}{e} \right) \quad (1)$$

$$\text{For } p\text{-type semiconductors: } \frac{1}{C^2} = \frac{2}{e\epsilon_r\epsilon_0 N_A} \left(-E + E_{fb} - \frac{k_B T}{e} \right) \quad (2)$$

where, C is the capacitance of the medium, e is the electronic charge (1.602×10^{-19} C), ϵ_r represents the relative dielectric constant, ϵ_0 depicts the free-space permittivity (8.85×10^{-14} F. cm⁻¹), k_B , E and T are the Boltzmann constant, applied potential (V) and absolute temperature (K), respectively. For an *n*-type semiconductor, E_{fb} remains nearer to the conduction band minimum (E_{CB}) and for a *p*-type material, it remains near the valance band maximum (E_{VB}). It is observed that for exfoliated g-C₃N₄ and pristine Bi₂S₃, the slopes of the M-S curves are positive,

implying n-type semiconducting behaviour. In contrary, for ZnFe_2O_4 , negative slope of the M-S curve indicates its p-type behaviour. The potentials ($E_{\text{fb}}|_{\text{NHE}}$), with respect to the normal hydrogen electrode (NHE), can be obtained from the measured $E_{\text{fb}}|_{\text{Ag/AgCl}}$ using the following equation [10]: $E_{\text{fb}}|_{\text{NHE}} = E_{\text{fb}}|_{\text{Ag/AgCl}} + E_{\text{Ag/AgCl}}^0 + 0.0592 \text{ pH}$, where, $E_{\text{Ag/AgCl}}^0 = 0.197 \text{ eV}$, $T = 25^\circ\text{C}$. Conventionally, pH of the electrolyte solution (0.5 M Na_2SO_4) is 5.5. So, the $E_{\text{fb}}|_{\text{NHE}}$ of the primary components are obtained as: $E_{\text{fb}}|_{\text{gCN}}: -1.46 \text{ eV}$, $E_{\text{fb}}|_{\text{Bi}_2\text{S}_3}: 0.27 \text{ eV}$ and $E_{\text{fb}}|_{\text{ZnFe}_2\text{O}_4}: 1.457 \text{ eV}$ vs. NHE. Now, the E_{CB} (E_{VB}) for an n (p) type semiconductor remains around 0.1–0.2 eV higher (lower) than the $E_{\text{fb}}|_{\text{NHE}}$. Therefore, following this conventional theory, the E_{VB} values for gCN and Bi_2S_3 are calculated as: -1.56 eV and 0.37 eV , respectively, whereas, for ZnFe_2O_4 , the E_{VB} is obtained as 1.557 eV . Finally, using the E_{g} values (determined for the UV-Vis DRS spectra) and the relationship $E_{\text{VB}} = E_{\text{CB}} - E_{\text{g}}$, the magnitudes of E_{VB} for gCN and Bi_2S_3 are: 1.28 eV and 1.75 eV , respectively. Similarly, the E_{CB} of ZnFe_2O_4 is -0.233 eV , calculated from the above formula.

3.1.5. Effect of microwave irradiation

The effect of microwave irradiation towards the variation of physicochemical and electronic properties of pristine g- C_3N_4 and composites have been analysed further in two ways. Firstly, the microwave treated g- C_3N_4 was analysed in terms of morphological, crystallographic and surface defects. The corresponding results are demonstrated in Figs. S2 (c-f). It can be observed that no morphological variations were introduced upon microwave treatment and the treated g- C_3N_4 sample retained its porous layered structure (Figs. S2(c,d)). The XRD spectra also exhibited no major crystalline structure variation (Fig. S2e). The Raman spectra of pristine and microwave treated g- C_3N_4 (Fig. S2f) show no significant differences. Characteristic peaks of g- C_3N_4 , i.e., 489 cm^{-1} , 554 cm^{-1} , 705 cm^{-1} , 762 cm^{-1} , 1234 cm^{-1} , 1555 cm^{-1} and 1700 cm^{-1} , can be identified for both the materials, which establishes that the s-triazine ring and C-N heterocycle structure of g- C_3N_4 are retained defect-free after microwave treatment. Specifically, the Raman shift at 705 cm^{-1} arises due to the breathing mode of the s-triazine ring and at 1234 cm^{-1} is associated with the lattice vibration of g- C_3N_4 framework [26,27]. Therefore, microwave irradiation imposes no physicochemical and electronic property variations in pristine g- C_3N_4 . The obtained results establish the proposition that pure carbon nitride structure is not a good microwave irradiation absorbing material [28]. However, microwave irradiation may have the potential to introduce self-structural defects into g- C_3N_4 framework during the occurrence of any insitu reaction. After the introduction of defects, the band structure and electronic configuration in pristine g- C_3N_4 framework might be modified to unevenly distribute the e^- charge and generate polarization effect. This phenomenon provides a strong driving force for excitation dissociation to obtain separated e^-/h^+ pairs and inhibit the photogenerated charge carrier recombination [18,28–30]. So, in the second study, effect of microwave irradiation has been monitored during the synthesis of the ternary heterojunction gCN/ ZnFe_2O_4 / Bi_2S_3 through the nucleation and growth of Bi_2S_3 on the dispersed gCN/ ZnFe_2O_4 composite. It is already discussed that formation of gCN/ ZnFe_2O_4 binary composite introduces structural defects in the g- C_3N_4 framework, through loss of N atoms. Introduction of defects distorts the internal distribution of e^- cloud into the g- C_3N_4 framework and the formation of low and high charge density regions generate a polarized electric field. This provides a strong driving force for the charge excitation dissociation to obtain separated e^- s and h^+ s, and inhibit the photogenerated charge carrier recombination. During microwave aided synthesis, the insitu nucleation and growth of Bi_2S_3 on gCN/ ZnFe_2O_4 introduce heteroatoms with different electronegativity (i.e., Bi and S) into the defective g- C_3N_4 network, which creates non-uniform charge distribution and asymmetric spin-density, resulting an induced polarization effect. Moreover, heterojunction formation also induces an internal

electric field along the depletion zone at the interface (positive to negatively charged region). In addition, ZnFe_2O_4 is an excellent absorber of microwave irradiation [31]. Therefore, the defect rich g- C_3N_4 induced polarization effects, heteroatom doping and creation of internal electric field within the heterojunction act synergistically to accelerate the transfer of photogenerated e^- s at the interface and inhibit the charge carrier recombination. The Raman spectra of binary gCN/ ZnFe_2O_4 composite identified most of the characteristic peaks of both the constituent components, such as 492 and 1280 cm^{-1} for g- C_3N_4 and 691 cm^{-1} for ZnFe_2O_4 [32,33]. However, compared to the pristine g- C_3N_4 , the absence of any peaks in the $705\text{--}712 \text{ cm}^{-1}$ region for the binary composite indicates the introduction of N-defects in the framework by intruding the s-triazine ring structure. In ZFO/BS(10) ternary composite, the characteristic peaks of Bi_2S_3 (at 130 and 983 cm^{-1}) [34, 35] can be clearly identified, along with all the typical peaks of gCN/ ZnFe_2O_4 . This indicates that no defect formation occurred during the microwave assisted synthesis of Bi_2S_3 on the gCN/ ZnFe_2O_4 composite. The slight shifting of some of the characteristic Raman peaks implies the charge transfer between Bi_2S_3 and gCN/ ZnFe_2O_4 and strong interfacial interaction. So, the generated polarization effects improve the charge separation and catalytic activities for the ternary composite which are in direct corroboration with the PL and electrochemical analysis (Fig. 3(c-e)). Besides, the morphological and crystallographic properties of g- C_3N_4 are unchanged for the both ternary (gCN/ ZnFe_2O_4 / Bi_2S_3) and binary (gCN/ ZnFe_2O_4) composites, as evidenced from the XRD and FESEM analysis (Fig. 1a and Fig. 2(c-e)).

3.2. Catalytic activity of the composite

3.2.1. Photocatalytic degradation of TCP

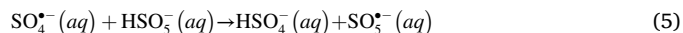
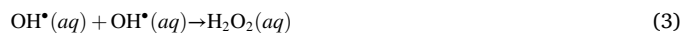
The TCP degradation is carried out using different combinations of catalyst/oxidant, either in presence or absence of visible light. As a representative catalyst, initially ZFO/BS(5) is employed. The generated kinetic profiles are presented in Fig. S3a. It is evident that in dark condition, the catalyst adsorbs negligible amount of TCP ($\sim 1.1\%$). In presence of visible light, the catalyst can effectively activate any oxidant. The combination of ZFO/BS(5) (0.25 g L^{-1}) and PMS (2 g L^{-1}) degrades 85% TCP, after 60 min visible light exposure, compared to only 12% and 10% TCP removal using sole PMS (no catalyst) and sole ZFO/BS(5) (no PMS), indicating synergistic and influencing interactions between the components. Also, the same ZFO/BS(5)/PMS combination degrades only 29.5% TCP, in absence of visible light. Therefore, visible light irradiation plays a vital role in the photoexcitation of e^-/h^+ pairs and subsequent activation of oxidants. With equal concentration of PDS and PMS (2 g L^{-1}), ZFO/BS(5) degrades 77% and 85% TCP, respectively. This study indicates that PMS is more reactive towards TCP oxidation, due to easy cleavage of its -O-O- bond and unsymmetrical molecular structure, leading to generation of large number of reactive radicals. Therefore, PMS was preferred as the superior oxidant for further degradation experiments.

Furthermore, a limiting Bi_2S_3 doping percentage provides the highest degradation efficiency. As shown in Fig. S3b, only catalyst, with no PMS and visible light exposure, results negligible TCP adsorption ($\sim 1.1\text{--}2\%$), for variation of Bi_2S_3 content from 5 wt% to 20 wt%. In presence of PMS and visible light, TCP degradation is enhanced from 88.4% to 98% for ZFO/BS(5) and ZFO/BS(10), respectively. Further doping of Bi_2S_3 slightly reduces TCP removal (81.3% for ZFO/BS(15) and 71.3% for ZFO/BS(20)). Lower Bi_2S_3 in the composite provides inadequate catalytic sites for capture and activation of PMS, lowering overall reactivity. Gradual doping of Bi_2S_3 introduces more active sites and improve the overall TCP degradation through activation of PMS, generation of radicals and adsorption of TCP. At higher Bi_2S_3 content, more recombination sites are generated in the non-hierarchical structure, imposing adverse effects on light harvesting and radical generation [36]. Therefore, in this work, ZFO/BS(10) is determined as the optimal catalyst and used in further studies. In comparison, 80% and 65% TCP degradations

are achieved in presence of gCN/ZnFe₂O₄/PMS and Bi₂S₃/PMS combinations, under visible light irradiation (Fig. S3c). The lower activities of both these systems are inferred to the most efficient separation of charge carriers in the ternary heterostructure. Moreover, the binary composite gCN/ZnFe₂O₄ shows stronger PMS activation, than Bi₂S₃, due to favourable charge separation and migration through the conductive framework.

3.2.2. Variation of catalyst and PMS dose

Optimization studies of the highest performing ratio, along with the catalyst and PMS dosage, are graphically depicted in Fig. S4. 1:4 wt ratio of the ZFO/BS(10):PMS exhibits the highest TCP degradation efficiency (Fig. S4a). So, this ratio was selected as the optimum for conducting further experiments. With this ratio, the increase in ZFO/BS(10) dosage till 0.25 gL⁻¹ improves TCP degradation up to 98.3% (Fig. S4b). Increase of ZFO/BS(10) dose beyond 0.25 gL⁻¹ leads to slight reduction in TCP degradation due to the agglomeration of catalyst particles along with increase in solution turbidity. Both these factors affect the transmission of incident irradiation in the medium, thus, imposing adverse effects on photoexcitation of the catalyst and related generation of ROS. The overall available active sites at the optimum dosage of ZFO/BS(10) (0.25 gL⁻¹) are sufficient to activate large number of PMS species and degrade considerable TCP molecules. Similarly, in presence of optimum dosage of ZFO/BS(10), increase of PMS concentration upto 1 gL⁻¹ results 98.9% TCP degradation and with further addition of PMS dose, the extent of degradation steadily decreases (Fig. S4c). Precisely, the available active sites at the optimum dose of ZFO/BS(10) cannot activate surplus amount of PMS species and thus, self-quenching becomes dominant (Eqs. (3–6)). Hence, the optimal dosage of ZFO/BS(10) and PMS are determined to be 0.25 gL⁻¹ and 1 gL⁻¹ for further photocatalytic experiments. The following reactions are involved in the radical quenching process at higher PMS concentrations:



3.2.3. Effect of different process parameters

Fig. S5a represents the visible light driven degradation trends for low to high initial concentration of TCP (C₀), in presence of optimal dose of catalyst (ZFO/BS(10): 0.25 gL⁻¹) and PMS (1 gL⁻¹). With variation of C₀ from 20 to 500 mgL⁻¹, the degradation efficiency decreases from 99.5% to 60% with 5.47 times decrease in k_{obs} (0.0831 min⁻¹ to 0.0152 min⁻¹). At higher C₀, more TCP molecules in the medium compete with the PMS species towards the active sites and generated radicals. Moreover, at large TCP concentration, greater number of intermediates and by-products are generated which consumes the radicals, lowering effective activity of the system. Therefore, higher C₀ lowers the TCP degradation, for constant PMS and catalyst dose. Still, significant TCP degradation (98.9–99.5%) can be obtained within C₀: 20–75 mgL⁻¹, in presence of optimal catalyst/PMS combination and visible light exposure.

The effect of pH on TCP degradation is investigated by varying the initial pH from 2 to 12 and the corresponding removals are represented in Fig. 4a. During the experiments, addition of optimal PMS lowers the feed solution pH. Quantitatively, for ZFO/BS(10) (0.25 gL⁻¹) and PMS (1 gL⁻¹), gradual rise of initial pH from 2 to 7 (pH of feed solution) increases TCP removal from 58% (k_{obs}: 0.0173 min⁻¹) to 98.9% (k_{obs}: 0.0772 min⁻¹). Gradual variation of initial pH from 8 to 10 decreases removal efficiency from 78.6% to 48.6%. Again, at highly alkaline pH (~12), 89.7% TCP degradation is observed (k_{obs}: 0.041 min⁻¹). This

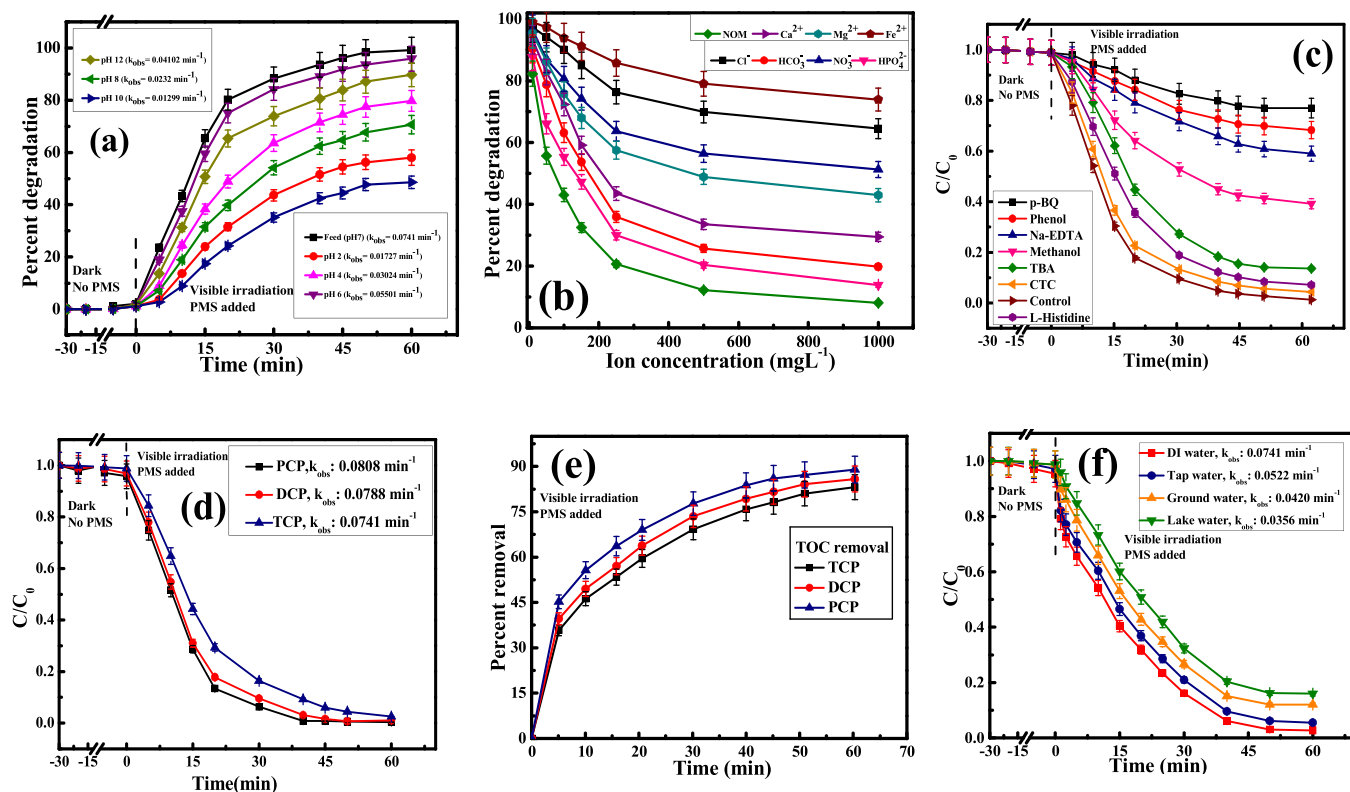


Fig. 4. Effect of different process parameters on degradation of TCP: (a) Initial solution pH; (b) Co-existing anions; (c) various radical scavengers; (d) degradation of different chlorophenols; (e) TOC removal of different chlorophenols, under identical operating conditions; (f) Effect of different water matrix on degradation of TCP. Reaction conditions: [TCP] = 50 mgL⁻¹, [catalyst] = 0.25 gL⁻¹, [PMS] = 1 gL⁻¹, initial solution pH: 7.0, Temperature [T] = 35 °C, visible light intensity: 80 W.

interesting influence of solution pH on TCP degradation is the outcome of the speciation of different reactive species. The pK_a of TCP is 6 [37] and the cationic, anionic and zwitterionic molecular structures of TCP dominate in the acidic, alkaline and neutral pH ranges, respectively. The pH_{PZC} of ZFO/BS (10) is determined at pH 5 which influences the electrostatic interaction between ionized reactants and the catalyst. Moreover, for PMS, the two pK_a values are pK_{a1} less than 0 and pK_{a2} : 9.5, i.e., PMS exists primarily as HSO_5^- below pH 9.5, and above that pH, SO_5^{2-} becomes the predominant form. Hence, at pH 2, the similar charge repulsion between the catalyst and ionized TCP molecules reduces overall adsorption and subsequent TCP degradation. Also, at highly acidic pH, dissociation of PMS is hindered due to high H^+ concentration and intense H-bonding with the peroxo ($-O-O-$) linkages. With the increase in solution pH (upto pH 7, with final pH ~ 5.8), the favourable associations among the positive or neutral TCP molecules and negatively charged catalyst surface boost the overall TCP degradation. Also, in neutral pH, concentration of $SO_4^{\bullet-}$ and OH^{\bullet} increases, resulting enhancement of overall catalytic activity of the system. However, in the alkaline range (initial solution pH 8–11, final pH 6.4–9.8), the similar anionic charges among the reactants and catalyst induce repulsive interaction, decreasing the overall degradation efficiency. In this pH range, the major ionic form of PMS becomes SO_5^{2-} which imposes strong repulsion towards negatively charged catalyst particles. Moreover, compared to HSO_5^- , activation of SO_5^{2-} is more difficult [3]. On the other hand, in this pH range, concentration of OH^{\bullet} increases, compared to $SO_4^{\bullet-}$ radicals. The reactivity of OH^{\bullet} towards TCP is weaker than that of $SO_4^{\bullet-}$ [38]. Overall, at initial pH of 10, the system shows the minimum reactivity. At highly alkaline pH (12), base-activation of PMS generates superoxide radicals ($O_2^{\bullet-}$) and singlet oxygen (O_2^1) which accelerate the TCP degradation due to higher oxidizing potentials (~ 1 V higher than O_2). This can surpass the repulsive interactions among the negatively charged catalyst and TCP ionic species. These highly reactive species ($O_2^{\bullet-}$ and O_2^1), along with surplus OH^{\bullet} radicals, can oxidize significant amount of TCP molecules [39]. So, overall, the TCP degradation efficiency is enhanced at neutral and highly alkaline pH. In this context, it should be specified that, use of buffer solution is avoided to maintain a constant solution pH as hike in the inorganic ion concentration in the reaction mixture may impose inconsistent effects towards the degradation performance. The reactions involved in PMS activation in basic solution are given as Eqs. S(2–12). The effects of leached ions on TCP degradation are studied at extremely acidic range (pH ~ 2). At this pH, the leached ion concentrations are determined as 0.1 mgL^{-1} , 0.085 mgL^{-1} and 0.07 mgL^{-1} for Fe, Zn and Bi, respectively. A separate TCP degradation study is carried out for homogeneous activation of PMS, in presence of visible light and specified concentrations of respective metal ions, at pH 2. After 60 min reaction under visible light, only 4.5% TCP was removed. Thus, it can be concluded that marginal leaching of constituent metal ions at extreme acidic pH (~ 2) is unable to substantially influence the PMS activation and corresponding TCP degradation can be neglected.

TCP degradation was conducted at three different temperatures, i.e., 25°C , 35°C and 55°C (298 K, 308 K and 328 K), respectively (Fig. S5b). It can be observed that, k_{obs} increases with temperature (0.0482 min^{-1} at 298 K to 0.0921 min^{-1} at 328 K) and are fitted perfectly in pseudo first order kinetic equation. Further, k_{obs} values are calculated as: $k_{obs} = A \exp(-E_a/RT)$, where, k_{obs} , A , E_a and R denote the pseudo first order rate constant at temperature T (K), frequency factor, activation energy of the reaction (kJ/mol) and ideal gas constant ($8.314 \text{ Jmol}^{-1}\text{K}^{-1}$), respectively. From this relation, E_a of the process is determined as 23.7 kJmol^{-1} ($>20 \text{ kJmol}^{-1}$), signifying that surface-confined chemical reaction of the adsorbed TCP molecules with PMS moieties is the rate controlling step, compared to the advective transport of the reactants and subsequent adsorption on the catalytic sites [4].

To determine the potential of the ZFO/BS(10)/PMS pair in presence of various foreign species, TCP degradation is carried out in mediums

having different ions and NOM (i.e., humic acid, HA). The overall inhibitory effect on TCP degradation varies in the order: $\text{NOM} > \text{HPO}_4^{2-} > \text{HCO}_3^- > \text{Ca}^{2+} > \text{Mg}^{2+} > \text{NO}_3^- > \text{Cl}^- > \text{Fe}^{2+} > \text{control}$ (Fig. 4b). HA molecules have quinone and semiquinone moieties, with strong radical quenching tendencies (Eqs. S(13,14)), along with increasing solution turbidity, blockage of catalyst sites and generation of other by-products. All these aspects affect the incident light harvesting capability of the catalyst and activity of radical species. Thus, TCP degradation is strongly inhibited in presence of HA. Both HPO_4^{2-} and HCO_3^- are strong scavengers of $SO_4^{\bullet-}$ and OH^{\bullet} , to generate weaker radicals (Eqs. S(15–20)), like, $\text{CO}_3^{\bullet-}$, HCO_3^{\bullet} and $\text{HPO}_4^{\bullet-}$. Moreover, these have strong buffering effects to modulate solution pH and both HPO_4^{2-} and HCO_3^- can replace surface -OH groups to form strong inner-sphere complexes with the metallic active sites on the catalyst [40–43]. The tendency to form inner-sphere interaction is stronger for HPO_4^{2-} than other employed anions. Therefore, both HPO_4^{2-} and HCO_3^- show significant inhibition towards TCP degradation (20.34% and 25.71% TCP removal for 500 mgL^{-1} of HPO_4^{2-} and HCO_3^- , respectively). This effect is also corroborative towards the formation of high-spin, inner-sphere, hydroxyl intermediates on the catalyst surface, as revealed from the XPS analysis. NO_3^- have lower scavenging tendencies to generate weaker radicals (NO_3^{\bullet} , NO_2^{\bullet}) and shows moderate inhibitory effects (Eqs. S(21–23)) (51.2% TCP removal at $1000 \text{ mgL}^{-1} \text{NO}_3^-$). On the contrary, Cl^- shows lower inhibition, due to replacement of OH^{\bullet} and $SO_4^{\bullet-}$ by Cl^{\bullet} (E^0 : 2.4 V), $\text{Cl}_2^{\bullet-}$ (E^0 : 2.1 V), OCl^{\bullet} (E^0 : 2.3 V), which contribute towards TCP removal. At higher concentration of Cl^- , minor inhibition is introduced due to high content of $\text{Cl}_2^{\bullet-}$ in the medium (Eqs. S(24–32)). Among different cations, Fe^{2+} shows the lowest inhibition, due to moderate homogeneous activation of PMS along with minor inhibition due to formation of precipitates. In contrast, both Ca^{2+} and Mg^{2+} show inhibition through blockage of active sites and formation of insoluble precipitates. Increase of Fe^{2+} dose from 10 mgL^{-1} to 1000 mgL^{-1} leads to TCP degradation from 98.9% to 73.9%, whereas for Mg^{2+} , this variation is from 95.5% to 42.9% and for Ca^{2+} , 93.3–29.47%, respectively. Overall, the effect of different ions on TCP degradation implies that radical based oxidation process is strongly active in the ZFO/BS(10)/PMS/Vis system.

3.2.4. Identification of reactive species

TCP degradation is performed in presence of various radical scavengers and represented in Fig. 4c. The relative quenching tendency and corresponding k_{obs} vary like: p-Benzoquinone (pBQ, k_{pBQ} : 0.0052 min^{-1}) > Phenol (PhOH, k_{PhOH} : 0.0074 min^{-1}) > EDTA-2Na ($k_{EDTA-2Na}$: 0.0083 min^{-1}) > Methanol (MeOH, k_{MeOH} : 0.0164 min^{-1}) > tert-butyl alcohol (TBA, k_{TBA} : 0.0386 min^{-1}) > L-Histidine (His, k_{His} : 0.0488 min^{-1}) > Carbon tetrachloride (CTC, k_{CTC} : 0.0586 min^{-1}) > control (no scavenger, $k_{control}$: 0.0741 min^{-1}). pBQ is a strong scavenger of $O_2^{\bullet-}$ ($k_{O_2^{\bullet-}/pBQ} = 1.0 \times 10^9 \text{ M}^{-1}\text{s}^{-1}$) and its highest suppression effect implies that $O_2^{\bullet-}$ is the strongest radical in the system. Being more hydrophobic than MeOH and TBA, PhOH (dielectric constant: 8, compared to 32.7 and 10.9 for MeOH and TBA, respectively) shows stronger quenching tendency towards surface bound $SO_4^{\bullet-}$ ($k_{SO_4^{\bullet-}/PhOH} = 8.8 \times 10^9 \text{ M}^{-1}\text{s}^{-1}$) and OH^{\bullet} ($k_{OH^{\bullet}/PhOH} = 6.6 \times 10^9 \text{ M}^{-1}\text{s}^{-1}$), than MeOH ($k_{SO_4^{\bullet-}/MeOH} = 1.6 \times 10^8 \text{ M}^{-1}\text{s}^{-1}$ and $k_{OH^{\bullet}/MeOH} = 9.7 \times 10^8 \text{ M}^{-1}\text{s}^{-1}$) and TBA ($k_{OH^{\bullet}/TBA} = 5.6 \times 10^8 \text{ M}^{-1}\text{s}^{-1}$ and $k_{SO_4^{\bullet-}/TBA} = 7.5 \times 10^5 \text{ M}^{-1}\text{s}^{-1}$). Therefore, surface-bound $SO_4^{\bullet-}$ and OH^{\bullet} impart stronger influences towards TCP degradation than the corresponding free radicals in the bulk. On the other hand, presence of α -Hs in the MeOH molecule imparts ability to trap both free $SO_4^{\bullet-}$ and OH^{\bullet} , compared to TBA, with no α -H, which can preferentially abstract free OH^{\bullet} radicals. Higher quenching tendency of MeOH than TBA indicates that $SO_4^{\bullet-}$ radicals play more active roles towards oxidation, than OH^{\bullet} radicals. Nonetheless, photo-generated h^+ s also contribute significantly towards TCP degradation, as suggested by the dominant inhibitory effect of EDTA-

$2\text{Na}(k_{\text{h}^+/\text{EDTA}-2\text{Na}} = 2.5 \times 10^7 \text{ M}^{-1}\text{s}^{-1})$. Finally, both His ($\text{O}_2^{\cdot-}$ scavenger with $k_{\text{O}_2^{\cdot-}/\text{His}} = 3.2 \times 10^7 \text{ M}^{-1}\text{s}^{-1}$) and CTC (solvated e^- scavenger with $k_{\text{e}^-/\text{CTC}} = 1.6 \times 10^6 \text{ M}^{-1}\text{s}^{-1}$) show negligible inhibitory effects, implying minor contributions of non-radical species ($\text{O}_2^{\cdot-}$ and solvated e^- s) towards TCP degradation. This study establishes that radical based ($\text{SO}_4^{\cdot-}$, OH^{\cdot} , $\text{O}_2^{\cdot-}$ and h^+) degradation pathway dominates during TCP degradation and non-radical mechanism shows negligible impacts.

To further establish the relative abundance of generated reactive radicals in solution, Electron Paramagnetic Resonance (EPR) analysis is conducted, employing DMPO and TEMPO as spin-trapping agents. The respective results are shown in Fig. 5. From the figure, it is evident that compared to the ZFO/BS(10)/PMS/dark combination, any other combination, i.e., PMS/Vis, ZFO/BS(10)/Vis and ZFO/BS(10)/PMS/Vis generates weak to strong peaks of radical-adducts. Specifically, the DMPO- $\text{O}_2^{\cdot-}$ intensity (sextet with 2:2:1:2:1:2 ratio) for ZFO/BS(10)/PMS/Vis is stronger than PMS/Vis and ZFO/BS(10)/Vis cases (Fig. 5a). Similarly, strong prominence of intensities can be observed for TEMPO- h^+ (triplet with 1:1:1 ratio, Fig. 5b), DMPO- OH^{\cdot} (quartet 1:2:2:1 ratio, Fig. 5c) and DMPO- $\text{SO}_4^{\cdot-}$ (sextet with 1:1:1:1:1:1 ratio, Fig. 5c), in presence of ZFO/BS(10)/PMS/Vis combination. On the other hand, the TEMPO- $\text{O}_2^{\cdot-}$ (triplet with 1:1:1 ratio) peak intensity is rather weak than its counterparts (Fig. 5d). This analysis firmly establishes that $\text{SO}_4^{\cdot-}$, OH^{\cdot} , $\text{O}_2^{\cdot-}$ and h^+ are significantly generated in ZFO/BS(10)/PMS/Vis system, under visible light. On the other hand, concentration of $\text{O}_2^{\cdot-}$ is rather small, compared to the other radicals.

3.2.5. Comparative degradation of different chlorophenols (CPs)

The ZFO/BS(10)/PMS combination is further employed towards the degradation of other chlorophenols (CPs), like, PCP, DCP along with TCP and the respective kinetic profiles of each CP is depicted in Fig. 4d. The results imply that all the CPs can be effectively degraded using the catalyst/PMS combination and with 60 min visible light treatment, 98.9% TCP, 99.2% DCP and 99.6% PCP degradation can be achieved.

Moreover, the order of degradation rate constants is given as: $k_{\text{PCP}}: 0.0808 \text{ min}^{-1} > k_{\text{DCP}}: 0.0788 \text{ min}^{-1} > k_{\text{TCP}}: 0.0741 \text{ min}^{-1}$. So, it is clear that multiple chlorine atoms in the CP molecule have strong influence on the degradation kinetics. This result can be interpreted as follows: (i) the initial step of degradation process involves the capturing of the contaminant molecules on catalyst surface. The graphitic framework and edge-exposed layered Bi_2S_3 structure provide abundant active sites that can drive the adsorption of pollutant molecules through strong intermolecular interactions, like, H-bonding, π - π interaction between the organic molecules and the residual amino and sulphide groups. CP molecules primarily form strong -H bonding through the -OH groups with the $-\text{NH}_2$ groups on the g- C_3N_4 surface and -SH groups on hydrated Bi_2S_3 layers, (ii) feasibility of formation, along with the stability and strength of this -H bonding are largely dependent on the alignment of the -OH and $-\text{NH}_2$ groups which is affected by the numbers and positions of the Cl atoms in the aromatic structure. With the increase of Cl atoms in the CP molecule, the steric hindrance increases, which affects the adsorption process, (iii) Also, with the increase of Cl atoms in the molecule, the σ electron withdrawing conductive effect becomes prominent, along with their involvement in the dechlorination process. Thus, more number of Cl atoms in the CP molecules decreases the rate of degradation as more radicals will be consumed in the dechlorination process. Moreover, the dechlorination step involves the attack of $\text{O}_2^{\cdot-}$ and $\text{SO}_4^{\cdot-}$ radicals. So, the more the number of Cl atoms in the CP molecules, lower will be the extent of degradation, (iv) increase of Cl atoms in the CP molecules decreases the overall stability of the metastable intermediates (π complexes) through diminished charge delocalisation, due to the e^- withdrawing tendency of the Cl atoms. Therefore, as the CP molecules become substituted with more Cl atoms, the energies of the transition states become higher and the rate of degradation decreases. The mineralization efficiency of the different CPs are determined by the time dependent TOC reduction study and the results are presented in the Fig. 4e. Quantitatively, 88.9%, 85.85% and 83.15% TOC removal efficiency are achieved for PCP, DCP and TCP after 60 min of the treatment

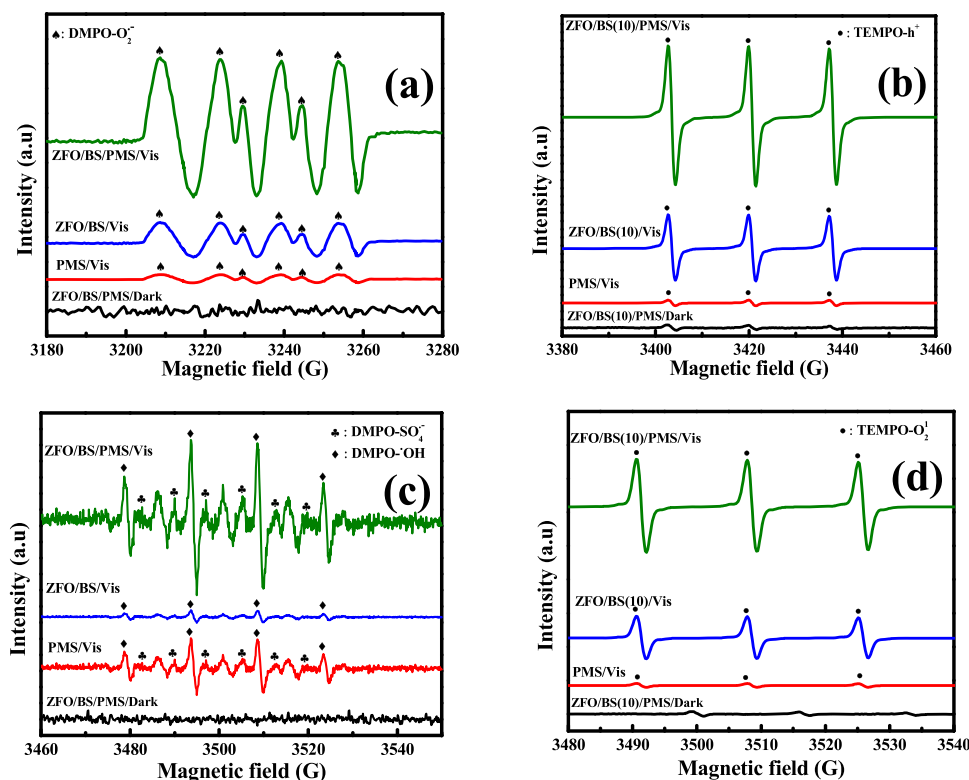


Fig. 5. EPR analysis of TCP solution in ZFO-BS(10)/PMS system: (a) DMPO- $\text{O}_2^{\cdot-}$ response; (b) TEMPO- h^+ response; (c) DMPO- OH^{\cdot} and DMPO- $\text{SO}_4^{\cdot-}$ response; (d) TEMPO- $\text{O}_2^{\cdot-}$ response.

time with ZFO/BS(10)/PMS/Vis irradiation system. Quite expectedly, the increased number of substituted Cl atoms in the phenolic moiety leads to the increment in the molecular stability of the intermediates which may have slightly decreased the extent of TOC removal. However, extent of TCP mineralization using the ZFO/BS(10) catalyst is quite significant, than similar other reported catalysts [44,45].

3.2.6. Effect of different water matrixes on TCP degradation

Kinetic studies of TCP degradation were carried out in different water matrixes including ultrapure water, municipal water, ground water and lake water. The physiochemical criterions of the water samples are reported in Table 1 and the removal efficiencies are depicted in Fig. 4f. Overall, 98.9% TCP was removed in ultrapure water, compared to 94.5%, 88% and 85% for municipal water, ground water and lake water, respectively. The lowering of TCP removal within different matrixes is attributed to the presence of dissolved ions and organics in higher concentration, along with turbidity and other interfering materials. Low concentration of dissolved ions and organics in municipal water exhibits minor inhibition towards TCP degradation. In contrast, groundwater and lake water contain higher density of TDS, ions and NOMs which impart lower to average inhibitory effects. These materials can scatter light significantly, with consumption of radicals and obstruction of catalyst pores. However, significant TCP is degraded in these matrixes (~85–95%). Therefore, the ZFO/BS(10)/PMS/Vis system can successfully remove TCP from actual surface water bodies.

3.3. Mechanistic insights of heterojunction formation and photocatalytic degradation

The ternary composite consists of three individual catalyst components, i.e., g-C₃N₄, ZnFe₂O₄ and Bi₂S₃, forming intimate heterojunction interface. Now, during the formation of the ternary composite, each of these materials influences the overall direction of e⁻ migration, along with affecting the electronic charge distribution and overall potential in the resultant composite. Traditionally, g-C₃N₄ and Bi₂S₃ are n-type semiconductors and their fermi levels (E_f) reside near the respective CBs. On the other hand, ZnFe₂O₄ is p-type semiconductor and has its fermi level near its VB. As a result, while forming heterojunction between ZnFe₂O₄ and g-C₃N₄, e⁻s will flow from the material with higher fermi level (g-C₃N₄) to the material with lower fermi level (ZnFe₂O₄). Due to this charge distribution, fermi level equilibrium will be obtained and a heterojunction will be formed where e⁻s in the CB of ZnFe₂O₄ tend to combine with the h⁺s in the VB of g-C₃N₄, forming a Z-scheme configuration. Also, interfacial band-bending will result due to the generated potential gradient (e.g., electric field), i.e., CB and VB edges of ZnFe₂O₄ (g-C₃N₄) will bend downwards (upwards) and a depletion zone will be created, along with an accompanying electric field, near the interface. Subsequently, when Bi₂S₃ is grown on the gCN/ZnFe₂O₄ binary

composite, e⁻s are transferred from the higher fermi level (Bi₂S₃) to lower fermi level (gCN/ZnFe₂O₄), till the fermi level equilibrium is established. Similar to the previous case, upward band bending occurs for Bi₂S₃ along with the downward band bending for gCN/ZnFe₂O₄ binary composite, with the formation of another depletion zone and induced electric field across the interface. Therefore, for the ternary heterostructure, a new fermi level equilibrium and overall internal electric field are established, resulting g-C₃N₄ as e⁻-rich, Bi₂S₃ as e⁻-deficient and ZnFe₂O₄ as the e⁻-mediator. This direction of e⁻ transfer is suitably reflected in the corresponding XPS spectrum of individual components and binary/ternary composites (Fig. S6). For the pristine g-C₃N₄, the high resolution XPS spectra of C1s contain two peaks at 284.5 eV (for C=C/C-C) and 288.2 eV (for N-C=N) which were shifted slightly at 284.8 eV and 288.6 eV, respectively, for the case of gCN/ZnFe₂O₄ binary composite (Fig. S6a). This indicates that during the formation of gCN/ZnFe₂O₄ binary composite, e⁻s have been donated by the g-C₃N₄ matrix. Similarly, for the gCN/ZnFe₂O₄ binary composite, the BEs of Zn2p (1021.8 eV and 1044.3 eV) and Fe2p (710.6 eV, 713.3 eV, 719.1 eV and 726.8 eV) are shifted slightly towards lower BEs compared to the nascent ZnFe₂O₄ with the peaks of Zn2p (1022.1 eV, 1044.7 eV) and Fe2p (710.9 eV, 713.6 eV, 719.3 eV and 727.1 eV), respectively (Figs. S6(b,c)). This observation implies that e⁻s are gained by ZnFe₂O₄ during the heterojunction formation. For pure Bi₂S₃, the Bi4f spectra contained two peaks at 158.8 eV and 164.1 eV, which shifted slightly to 159.2 eV and 164.4 eV in the ZFO/BS composite, implying the loss of e⁻s from the Bi₂S₃ for the ternary heterojunction formation (Fig. S6d). On the other hand, in the ZFO/BS composite, the peaks of Zn2p (1021.5 eV and 1043.8 eV) and Fe2p (710.1 eV, 712.8 eV, 718.4 eV and 726.3 eV) were generated through slight shifting towards lower BEs, compared to the nascent binary composite gCN/ZnFe₂O₄ (Figs. S6(b,c)), which establish that during heterojunction formation, the binary composite accepts e⁻s from Bi₂S₃. So, the final ternary heterojunction composite ZFO/BS can improvise either an efficient n-p-n dual type-II or dual Z-scheme heterojunction configuration.

Formation of dual type-II heterojunction involves the transfer of e⁻s from the CBs of both g-C₃N₄ and ZnFe₂O₄ towards the CB of Bi₂S₃ (i.e., downhill direction), with the simultaneous migration of h⁺s from the VBs of both ZnFe₂O₄ and Bi₂S₃ to the VB of g-C₃N₄ (i.e., uphill direction) (Fig. 6a). Therefore, the e⁻ (h⁺) density will be higher in the CB (VB) of Bi₂S₃ (g-C₃N₄). This spatial separation of the photogenerated e⁻/h⁺ pairs is also thermodynamically feasible due to the internal electric field generated by the charge migration and corresponding band alignment. Still, it is not practically advantageous because the oxidation and reduction reactions take place in the semiconductors with lowest redox potentials. In the present study, the E_{CB} of Bi₂S₃ is 0.37 eV and the e⁻s in the CB of Bi₂S₃ are unable to reduce the O₂ molecules to generate adequate O₂^{•-} (E_{O₂/O₂^{•-} : - 0.33 eV vs. NHE). So, the availability of O₂^{•-} within the system will be less probable for the n-p-n type-II heterojunction. This speculation directly contradicts the experimental results where O₂^{•-} was identified as the primary reactive species. On the contrary, in the direct dual type Z-scheme configuration (Fig. 6b), e⁻s in the CBs of ZnFe₂O₄ and Bi₂S₃ tends to combine with the h⁺s in the VBs of g-C₃N₄ and ZnFe₂O₄, respectively. So, the charges are mostly gathered on the CB of g-C₃N₄ and VB of Bi₂S₃, respectively. This would result in an efficient splitting of e⁻/h⁺ pairs on the semiconductors containing its highest reduction and oxidation potentials. Also, this charge migration is physically more favourable than type-II configuration because of electrostatic attraction between nearest e⁻s and h⁺s. For this material, the highly reductive e⁻s in the CB of g-C₃N₄ (E_{CB}: -1.56 eV) are able to reduce O₂ molecules to O₂^{•-} (E_{O₂/O₂^{•-} : - 0.33 eV vs. NHE). Additionally, the h⁺s in the VB of Bi₂S₃ (E_{VB}: 1.75 eV) are highly reactive and can potentially oxidize the adsorbed TCP molecules. Now, both E_{OH[•]/OH⁻} (1.99 eV vs. NHE) and E_{OH[•]/H₂O} (2.27 eV vs. NHE) are higher than the E_{VB} of Bi₂S₃ which suggest that OH[•] is not generated by oxidation of}}

Table 1
Overall characteristics of employed water samples.

Parameters	Ultrapure water	Municipal water	Groundwater	Lake water
pH	6.5 ± 0.7	7.5 ± 0.7	7.1 ± 0.5	6.1 ± 0.8
TOC (mg L ⁻¹)	–	14.5 ± 0.2	23.4 ± 0.5	55.1 ± 0.5
Chloride (Cl ⁻ , mg L ⁻¹)	–	6.7 ± 0.2	9.6 ± 0.3	21.3 ± 0.3
Sulfate (SO ₄ ²⁻ , mg L ⁻¹)	–	25.5 ± 0.4	38.5 ± 0.5	45.2 ± 0.5
Bicarbonate (HCO ₃ ⁻ , mg L ⁻¹)	–	85 ± 6	123 ± 3.5	178 ± 3.6
Nitrate (NO ₃ ⁻ , mg L ⁻¹)	–	1.35 ± 0.07	1.29 ± 0.05	0.59 ± 0.02
TDS (mg L ⁻¹)	–	200 ± 20	685 ± 15	375 ± 50
Total Fe (mg L ⁻¹)	–	3.4 ± 1.8	4.4 ± 4.5	5.5 ± 1.7

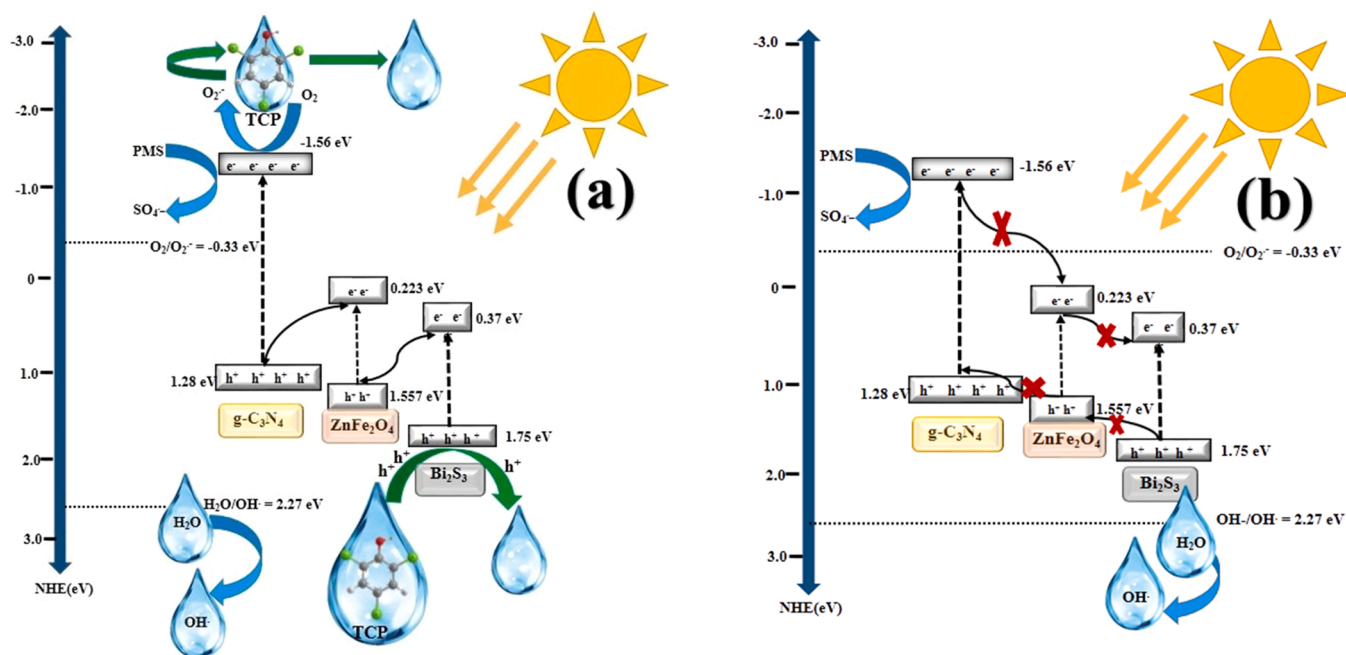


Fig. 6. Schematic diagram of (a) dual Z-scheme ZFO/BS, (b) general type II heterojunction for the photocatalytic degradation of TCP.

OH^- anions or H_2O molecules by the h^+ s, rather, through decomposition of PMS species (i.e., HSO_5^- anions) by e^- transfer using surface-bound redox cycles which generate large amount of $\text{SO}_4^{\bullet-}$. These can subsequently form OH^{\bullet} , as the $E_{\text{SO}_4^{\bullet-}/\text{SO}_4^{2-}}^0$ (2.5–3.1 eV) is higher than $E_{\text{OH}^{\bullet}/\text{H}_2\text{O}}^0$. So, along with the supportive evidences from the radical scavenging experiments, construction of dual Z-scheme heterojunction is highly probable for this case, as schematically depicted in Fig. 6.

The XPS analysis of reacted and nascent ZFO/BS composite indicates that redox interconversions of the surface metal atoms are active during the catalytic reactions. The process starts with the dissociation of PMS moieties (i.e., HSO_5^- ions), transforming to SO_5^{2-} ions along with the generation of $\text{SO}_5^{\bullet-}$, $\text{SO}_4^{\bullet-}$ and $\text{O}_2^{\bullet-}$ (Eqs. S(33–37)). The HSO_5^- ions would react with $\text{Zn}^{2+}|_{\text{surf.}}$ to produce transient $\text{Zn}^{3+}|_{\text{surf.}}$, along with $\text{SO}_4^{\bullet-}$ in the medium. This short-lived $\text{Zn}^{3+}|_{\text{surf.}}$ can react with H_2O molecules to produce OH^{\bullet} , with simultaneous conversion into $\text{Zn}^{2+}|_{\text{surf.}}$. On the other hand, $\text{Zn}^{2+}|_{\text{surf.}}$ also can generate $\text{Zn}^+|_{\text{surf.}}$ through reaction with HSO_5^- ions (Eqs. S(38–41)). This sequence is energetically realizable as the redox potential $E_{\text{Zn}^{2+}/\text{Zn}^+}^0$ (1.45 V) is between $E_{\text{HSO}_5^-/\text{SO}_5^{2-}}^0$ (1.1 V) and both $E_{\text{HSO}_5^-/\text{HSO}_4^-}^0$ (1.8 V) and $E_{\text{HSO}_5^-/\text{SO}_4^{\bullet-}}^0$ (2.8–3.1 V), respectively. However, $\text{Fe}^{3+}|_{\text{surf.}}$ ions are unable to be reduced by HSO_5^- as the $E_{\text{Fe}^{2+}/\text{Fe}^{3+}}^0$ (0.77 V) is weaker than the redox potential of HSO_5^- . However, the already formed $\text{O}_2^{\bullet-}$ radicals and transient $\text{Zn}^+|_{\text{surf.}}$ can reduce $\text{Fe}^{3+}|_{\text{surf.}}$ to $\text{Fe}^{2+}|_{\text{surf.}}$ state (Eqs. S(42,43)). The originated $\text{Fe}^{2+}|_{\text{surf.}}$ can activate PMS and generate $\text{SO}_4^{\bullet-}$ (Eqs. S(44–46)) through direct e^- transfer. In this process, the adsorbed H_2O molecules couple with the $\text{Zn}^{2+}|_{\text{surf.}}$ and $\text{Fe}^{2+}|_{\text{surf.}}$ ions to form invariant hydroxyl intermediates $\text{Zn}^{2+}|_{\text{surf.}} - (\text{OH}^-)$ and $\text{Fe}^{2+}|_{\text{surf.}} - (\text{OH}^-)$ which attack the captured PMS species to generate transient, high-spin, inner-sphere and metastable hydroxyl complexes $\text{M}^{2+}|_{\text{surf.}} - (\text{OH})(\text{OSO}_3^-)$ (M: Zn, Fe). Subsequently, these reactive complexes can interact with the TCP moieties via an inner-sphere complexation mechanism and transfer of e^- s to the catalyst surface. Upon generation of the $\text{M}^{2+}|_{\text{surf.}} - (\text{OH})(\text{OSO}_3^-)$ intermediates, one e^- is conveyed to the captured HSO_5^- ions to form $\text{SO}_4^{\bullet-}$ radicals, with subsequent oxidation of $\text{M}^{2+}|_{\text{surf.}}$ to

$\text{M}^{3+}|_{\text{surf.}}$ (M: Zn, Fe) (Eqs. S(47–54)). Next, all of the adsorbed TCP species are oxidized through one e^- transfer towards the HSO_5^- . Likewise, each of the captured HSO_5^- acquires two e^- s (from $\text{M}^{2+}|_{\text{surf.}}$ ions and bound TCP molecules). In this context, it can be mentioned that the large density of active sites overcomes the energy barrier to drive the extremely transient redox conversion of $\text{Zn}^{2+}|_{\text{surf.}}$ to $\text{Zn}^{3+}|_{\text{surf.}}$. On the other hand, Bi_2S_3 in the composite also activates the PMS and generates $\text{SO}_4^{\bullet-}$ radicals, through direct e^- transfer process. In this case, the $\text{Bi}^{3+}|_{\text{surf.}}$ ions can form metastable intermediate $\text{Bi}^{3+}|_{\text{surf.}} - (\text{OH})(\text{OSO}_3^-)$ which tends to transfer one e^- to the neighbouring PMS molecule, generating $\text{SO}_4^{\bullet-}$ and $\text{Bi}^{4+}|_{\text{surf.}}$ state. Also, the $\text{Bi}^{3+}|_{\text{surf.}}$ can reduce the $\text{Fe}^{3+}|_{\text{surf.}}$ to generate $\text{Fe}^{2+}|_{\text{surf.}}$, along with self-oxidation to $\text{Bi}^{4+}|_{\text{surf.}}$ (Eqs. S(55–60)). Next, the adsorbed TCP molecules transfer e^- s towards the HSO_5^- and get oxidized. Moreover, the residing $\text{O}_2^{\bullet-}$ radicals may react with the HSO_5^- ions to produce O_2^1 species (Eqs. S(61–63)). Lastly, for the non-radical based process involving surface mediated e^- transfer, the conductive graphitic framework and hierarchical Bi_2S_3 layered arrangement act as e^- bridge to transfer e^- density of the TCP molecules (e^- donor) to the adsorbed PMS moieties (e^- acceptor). As a result, the TCP molecules become e^- scarce and responsive to electrophilic reaction by the major reactive species ($\text{SO}_4^{\bullet-}$, OH^{\bullet} , $\text{O}_2^{\bullet-}$, O_2^1 , h^+) (Eq. S64).

In this regard, the merit of formation of the ternary composite and introduction of ZnFe_2O_4 in the structure, compared to any of the binary composite can be established through the following points. Firstly, formation of binary composites between any two of the three primary components (i.e., $\text{gCN}/\text{ZnFe}_2\text{O}_4$, $\text{ZnFe}_2\text{O}_4/\text{Bi}_2\text{S}_3$ and $\text{gCN}/\text{Bi}_2\text{S}_3$) leads to efficient charge separation (Fig. S7). In fact, formation of Z-scheme configuration is highly feasible for all the three cases. Still, generation of ternary heterojunction remarkably improves the overall charge separation efficiency and harvesting of incident visible light irradiation, as supported by the PL and EIS analysis, along with the photocurrent responses. Moreover, the catalytic activities of the ZFO/BS composite is superior than any of the binary composites, due to the availability and separation of photogenerated e^-/h^+ pairs and subsequent generation of abundant reactive radicals. Formation of ternary composite with dual Z-

molecular weight compounds can be oxidized to aliphatic aldehydes and carboxylic acids such as intermediates I_{12} , I_{13} , I_{14} . It is observed that at the end of reaction, lower molecular weight organic compounds, CO_2 and H_2O are generated through complete degradation of the intermediates. Though exact disintegration mechanism of small and transient molecules cannot be established, TOC reduction and finding of some of the smaller compounds indicate the overall proposed degradation pathways of TCP as just a glimpse of the comprehensive mechanism. Details of the generated intermediates (i.e., formula, m/z values and chemical structures) are given in Table S1, along with the relevant LCMS spectra in Figs. S8(a-d).

3.5. Comparative analysis with existing studies

To evaluate the usefulness and suitability of the developed ternary catalyst, with respect to other state-of-the-art materials, a detailed comparative study has been undertaken and the details are summarized in Table S2. Each of the already reported catalysts involves high temperature calcination and/or hydrothermal method for synthesis, which are both energy and time intensive, compared to the microwave assisted synthesis scheme which requires much less energy input and synthesis time. Also, the reported doses of catalyst (ZFO/BS(10): 0.25 gL^{-1}) and PMS (1.0 gL^{-1}) are smaller than most of the reported values, applied for complete removal of 50 mgL^{-1} TCP. Moreover, the obtained k_{obs} (0.0741 min^{-1}) is highest among most of the recently developed systems. Thus, the synthesized catalyst (ZFO/BS(10)) is highly effective towards degradation of TCP (with $>80\%$ mineralization), which proves its suitability towards actual process applications.

Furthermore, the merits of microwave assisted synthesis method can also be established from the perspective of overall cost analysis. In the synthesis of the ternary composite, either through microwave assisted or hydrothermal based methods, the total cost consists of precursor cost and energy cost for reaction, calcination and drying of the materials. Detailed calculations (refer section S9) show that for production of ZFO/BS(10) composite through microwave assisted procedure, Rs. 6.75 g^{-1} (0.09\$ approx.) needs to be expended, compared to Rs. 29.11 g^{-1} (0.39\$ approx.), when synthesized using hydrothermal technique.

4. Stability and reusability

To determine the catalyst reusability, sequential set of degradation studies are conducted with the retrieved catalyst from previous sets. The substantial magnetic susceptibility of the material aids its efficient separation. The TCP degradation efficiency of the reutilized catalyst is shown in Fig. 8a and it shows 85.6% TCP degradation upto 4th cycle, implying higher stability and activity of the catalyst. However, in the 5th cycle, the degradation extent is reduced to 81.5% which is due to the gradual adsorption of organic molecules on the active sites and loss of constituent atoms. Further, the leaching of Zn, Fe and Bi ions from the

ZFO/BS catalyst after each cycle is determined. The leached concentrations after 5th cycle are 0.09 mgL^{-1} , 0.06 mgL^{-1} and 0.04 mgL^{-1} for Fe, Zn and Bi, respectively, as presented in Fig. 8b. Leaching concentration of every metal ion is below the effluent discharge limit [47]. So, it can be inferred that the spent catalyst produces no significant heavy metal pollution to the surface water even after its exhaustive cyclic use, and no post-treatment of the decontaminated water is required. Moreover, after each regeneration cycle, the catalyst is recovered and investigated using XRD to determine any variation in crystallographic structure. The results are shown in Fig. 8c which clearly exhibits no alteration of crystallographic framework, after multiple cycles of reuse. This result establishes that the ZFO/BS(10) composite is structurally robust and stable. The slight lowering of peak intensities can be ascribed to the minor leaching of constituent metal atoms and deposition of organic layer on the catalyst surface.

5. Conclusion

A simple, microwave assisted synthesis method was developed to prepare a ternary dual Z-scheme photocatalyst ZFO/BS with excellent visible light driven TCP degradation capability, in conjunction with PMS. Doping of Bi_2S_3 on $\text{gCN}/\text{ZnFe}_2\text{O}_4$ significantly improved the photocatalytic activity, forming an n-p-n heterojunction and the composite with 10 wt% Bi_2S_3 exhibited highest reactivity. Bulk g- C_3N_4 acted as a sacrificial oxidizing agent and conductive supporting matrix, along with imparting magnetic property. 98.9% TCP degradation was obtained using 0.25 gL^{-1} catalyst and 1.0 gL^{-1} PMS, with 60 mins visible light exposure. Excellent photocatalytic activity was attributed to successful formation of dual Z-scheme heterojunction, inhibition of photogenerated e^-/h^+ recombination, interconversion of surface-bound redox cycles, like, $\text{Fe}^{2+/3+}_{\text{surf}}$, $\text{Zn}^{2+/2+}_{\text{surf}}$ and $\text{Bi}^{3+/4+}_{\text{surf}}$, and charge migration through transient intermediates. Detailed TCP degradation pathway was proposed based on intermediate analysis. Magnetic susceptibility and structural integrity of the composite impart high recoverability for five continuous cycles. The above results indicate that ternary ZFO/BS(10) composite has great potential for oxidative mineralization of emerging EDCs and the synthesis method can be adopted for design and preparation of different metal chalcogenide based semiconductor heterojunctions.

CRedit authorship contribution statement

Poulomi Sarkar: Conceptualization, Experimentation, Methodology, Software, Validation, Writing, Editing – original draft preparation. **Sirshendu De:** Investigation, Reviewing and editing, Supervision. **Sudarsan Neogi:** Investigation, Reviewing and editing, Conceptualization, Supervision.

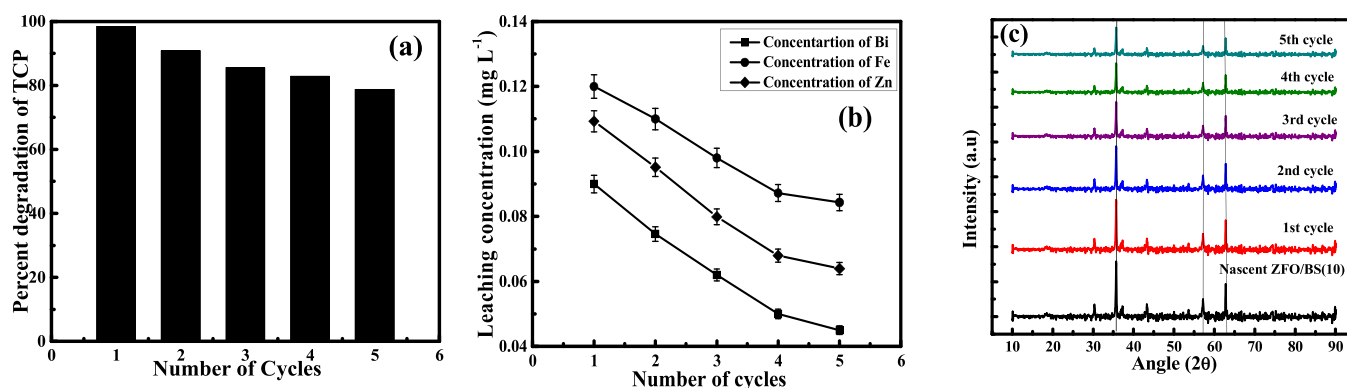


Fig. 8. (a). Reusability studies of the ZFO/BS(10); (b) leached ion concentrations after consecutive cycles; (c) XRD study for the regenerated catalysts.

Declaration of Competing Interest

The authors declare that they have no known competing financial interests or personal relationships that could have appeared to influence the work reported in this paper.

Acknowledgement

This work is supported by a grant from the Department of Science and Technology, Government of India, under the scheme no. DST/TM/WTI/WIC/2K17/84(G), Dt. 15–01-2019. Any opinions, findings and conclusions expressed in this paper are those of the authors. The authors would also like to acknowledge Mr. Debashis Roy, Department of Chemical Engineering, IIT Kharagpur, for helping with characterization and insightful discussions.

Appendix A. Supporting information

Supplementary data associated with this article can be found in the online version at [doi:10.1016/j.apcatb.2022.121165](https://doi.org/10.1016/j.apcatb.2022.121165).

References

- [1] E. Diamanti-Kandarakis, J.-P. Bourguignon, L.C. Giudice, R. Hauser, G.S. Prins, A. M. Soto, R.T. Zoeller, A.C. Gore, Endocrine-disrupting chemicals: an endocrine society scientific statement, *Endocr. Rev.* 30 (2009) 293–342, <https://doi.org/10.1210/er.2009-0002>.
- [2] W.-D. Oh, Z. Dong, T.-T. Lim, Generation of sulfate radical through heterogeneous catalysis for organic contaminants removal: current development, challenges and prospects, *Appl. Catal. B Environ.* 194 (2016) 169–201, <https://doi.org/10.1016/j.apcatb.2016.04.003>.
- [3] J. Wang, S. Wang, Activation of persulfate (PS) and peroxymonosulfate (PMS) and application for the degradation of emerging contaminants, *Chem. Eng. J.* 334 (2018) 1502–1517, <https://doi.org/10.1016/j.cej.2017.11.059>.
- [4] F. Ghanbari, M. Moradi, Application of peroxymonosulfate and its activation methods for degradation of environmental organic pollutants: review, *Chem. Eng. J.* 310 (2017) 41–62, <https://doi.org/10.1016/j.cej.2016.10.064>.
- [5] A. Sudhaik, P. Raizada, P. Shandilya, P. Singh, Magnetically recoverable graphitic carbon nitride and NiFe₂O₄ based magnetic photocatalyst for degradation of oxytetracycline antibiotic in simulated wastewater under solar light, *J. Environ. Chem. Eng.* 6 (2018) 3874–3883, <https://doi.org/10.1016/j.jece.2018.05.039>.
- [6] S. Huang, Y. Xu, M. Xie, H. Xu, M. He, J. Xia, L. Huang, H. Li, Synthesis of magnetic CoFe₂O₄/g-C₃N₄ composite and its enhancement of photocatalytic ability under visible-light, *Colloids Surf. A Physicochem. Eng. Asp.* 478 (2015) 71–80, <https://doi.org/10.1016/j.colsurfa.2015.03.035>.
- [7] N. Liang, J. Zai, M. Xu, Q. Zhu, X. Wei, X. Qian, Novel Bi₂S₃/Bi₂O₂CO₃ heterojunction photocatalysts with enhanced visible light responsive activity and wastewater treatment, *J. Mater. Chem. A* 2 (2014) 4208, <https://doi.org/10.1039/c3ta13931j>.
- [8] A. Kumar, Y. Kuang, Z. Liang, X. Sun, Microwave chemistry, recent advancements, and eco-friendly microwave-assisted synthesis of nanoarchitectures and their applications: a review, *Mater. Today Nano* 11 (2020), 100076, <https://doi.org/10.1016/j.mtnano.2020.100076>.
- [9] A. Kubiak, Z. Bielan, M. Kubacka, E. Gabała, A. Zgoła-Grzeskowiak, M. Janczarek, M. Zalas, A. Zielińska-Jurek, K. Siwińska-Ciesielczyk, T. Jesionowski, Microwave-assisted synthesis of a TiO₂-CuO heterojunction with enhanced photocatalytic activity against tetracycline, *Appl. Surf. Sci.* 520 (2020), 146344, <https://doi.org/10.1016/j.apsusc.2020.146344>.
- [10] P. Sarkar, D. Roy, B. Bera, S. De, S. Neogi, Efficient photocatalytic degradation of ciprofloxacin using novel dual Z-scheme gCN/CuFe₂O₄/MoS₂ mediated peroxymonosulfate activation, *Chem. Eng. J.* 430 (2022), 132834, <https://doi.org/10.1016/j.cej.2021.132834>.
- [11] Y. Ma, E. Liu, X. Hu, C. Tang, J. Wan, J. Li, J. Fan, A simple process to prepare few-layer g-C₃N₄ nanosheets with enhanced photocatalytic activities, *Appl. Surf. Sci.* 358 (2015) 246–251, <https://doi.org/10.1016/j.apsusc.2015.08.174>.
- [12] J. Lu, Q. Han, X. Yang, L. Lu, X. Wang, Microwave-assisted synthesis and characterization of 3D flower-like Bi₂S₃ superstructures, *Mater. Lett.* 61 (2007) 2883–2886, <https://doi.org/10.1016/j.matlet.2007.01.071>.
- [13] J. Wu, F. Qin, G. Cheng, H. Li, J. Zhang, Y. Xie, H.-J. Yang, Z. Lu, X. Yu, R. Chen, Large-scale synthesis of bismuth sulfide nanorods by microwave irradiation, *J. Alloy. Compd.* 509 (2011) 2116–2126, <https://doi.org/10.1016/j.jallcom.2010.10.160>.
- [14] Y. Wang, H. Sun, H.M. Ang, M.O. Tade, S. Wang, Facile synthesis of hierarchically structured magnetic MnO₂/ZnFe₂O₄ hybrid materials and their performance in heterogeneous activation of peroxymonosulfate, *ACS Appl. Mater. Interfaces* 6 (2014) 19914–19923, <https://doi.org/10.1021/am505309b>.
- [15] K.C. Christoforidis, T. Montini, E. Bontempi, S. Zafeiratos, J.J.D. Jaén, P. Fornasiero, Synthesis and photocatalytic application of visible-light active β -Fe₂O₃/g-C₃N₄ hybrid nanocomposites, *Appl. Catal. B Environ.* 187 (2016) 171–180, <https://doi.org/10.1016/j.apcatb.2016.01.013>.
- [16] T. Danno, D. Nakatsuka, Y. Kusano, H. Asaoka, M. Nakanishi, T. Fujii, Y. Ikeda, J. Takada, Crystal structure of β -Fe₂O₃ and topotactic phase transformation to α -Fe₂O₃, *Cryst. Growth Des.* 13 (2013) 770–774, <https://doi.org/10.1021/cg301493a>.
- [17] M. Sumathi, A. Prakasam, P.M. Anbarasan, A facile microwave stimulated g-C₃N₄/α-Fe₂O₃ hybrid photocatalyst with superior photocatalytic activity and attractive cycling stability, *J. Mater. Sci. Mater. Electron.* 30 (2019) 10985–10993, <https://doi.org/10.1007/s10854-019-01439-1>.
- [18] J. Tan, N. Tian, Z. Li, J. Li, X. Yao, M. Vakili, Y. Lu, T. Zhang, Intrinsic defect engineering in graphitic carbon nitride for photocatalytic environmental purification: a review to fill existing knowledge gaps, *Chem. Eng. J.* 421 (2021), 127729, <https://doi.org/10.1016/j.cej.2020.127729>.
- [19] S. Patnaik, K.K. Das, A. Mohanty, K. Parida, Enhanced photo catalytic reduction of Cr (VI) over polymer-sensitized g-C₃N₄/ZnFe₂O₄ and its synergism with phenol oxidation under visible light irradiation, *Catal. Today* 315 (2018) 52–66, <https://doi.org/10.1016/j.cattod.2018.04.008>.
- [20] Y. Yao, Y. Cai, F. Lu, J. Qin, F. Wei, C. Xu, S. Wang, Magnetic ZnFe₂O₄-C₃N₄ hybrid for photocatalytic degradation of aqueous organic pollutants by visible light, *Ind. Eng. Chem. Res.* 53 (2014) 17294–17302, <https://doi.org/10.1021/ie503437z>.
- [21] B. Yang, K. Lv, Q. Li, J. Fan, M. Li, Photosensitization of Bi₂O₂CO₃ nanoplates with amorphous Bi₂S₃ to improve the visible photoreactivity towards NO oxidation, *Appl. Surf. Sci.* 495 (2019), 143561, <https://doi.org/10.1016/j.apsusc.2019.143561>.
- [22] X. Chen, Q. Li, J. Li, J. Chen, H. Jia, Modulating charge separation via in situ hydrothermal assembly of low content Bi₂S₃ into UiO-66 for efficient photothermocatalytic CO₂ reduction, *Appl. Catal. B Environ.* 270 (2020), 118915, <https://doi.org/10.1016/j.apcatb.2020.118915>.
- [23] Y. Fu, X. Wang, Magnetically separable ZnFe₂O₄-graphene catalyst and its high photocatalytic performance under visible light irradiation, *Ind. Eng. Chem. Res.* 50 (2011) 7210–7218, <https://doi.org/10.1021/ie200162a>.
- [24] H. Tian, M. Liu, W. Zheng, Applied catalysis B: environmental constructing 2D graphitic carbon nitride nanosheets / layered MoS₂ / graphene ternary nanojunction with enhanced photocatalytic activity, *Appl. Catal. B Environ.* 225 (2018) 468–476, <https://doi.org/10.1016/j.apcatb.2017.12.019>.
- [25] H.Y. Hafeez, S.K. Lakhera, N. Narayanan, S. Harish, Y. Hayakawa, B.-K. Lee, B. Neppolian, Environmentally sustainable synthesis of a CoFe₂O₄-TiO₂/rGO ternary photocatalyst: a highly efficient and stable photocatalyst for high production of hydrogen (solar fuel), *ACS Omega* 4 (2019) 880–891, <https://doi.org/10.1021/acsomega.8b03221>.
- [26] Y. Wang, W. Yang, X. Chen, J. Wang, Y. Zhu, Photocatalytic activity enhancement of core-shell structure g-C₃N₄/TiO₂ via controlled ultrathin g-C₃N₄ layer, *Appl. Catal. B Environ.* 220 (2018) 337–347, <https://doi.org/10.1016/j.apcatb.2017.08.004>.
- [27] X. Bai, L. Wang, Y. Wang, W. Yao, Y. Zhu, Enhanced oxidation ability of g-C₃N₄ photocatalyst via C60 modification, *Appl. Catal. B Environ.* 152–153 (2014) 262–270, <https://doi.org/10.1016/j.apcatb.2014.01.046>.
- [28] Y. Liu, X. Guo, Z. Chen, W. Zhang, Y. Wang, Y. Zheng, X. Tang, M. Zhang, Z. Peng, R. Li, Y. Huang, Microwave-synthesis of g-C₃N₄ nanoribbons assembled seaweed-like architecture with enhanced photocatalytic property, *Appl. Catal. B Environ.* 266 (2020), 118624, <https://doi.org/10.1016/j.apcatb.2020.118624>.
- [29] W. Iqbal, B. Yang, X. Zhao, M. Rauf, M. Waqas, Y. Gong, J. Zhang, Y. Mao, Controllable synthesis of graphitic carbon nitride nanomaterials for solar energy conversion and environmental remediation: the road travelled and the way forward, *Catal. Sci. Technol.* 8 (2018) 4576–4599, <https://doi.org/10.1039/C8CY01061G>.
- [30] X. Bai, T. Jia, X. Wang, S. Hou, D. Hao, Bingjie-Ni, High carrier separation efficiency for a defective g-C₃N₄ with polarization effect and defect engineering: mechanism, properties and prospects, *Catal. Sci. Technol.* 11 (2021) 5432–5447, <https://doi.org/10.1039/D1CY00595B>.
- [31] A. Houbi, Z.A. Aldashevich, Y. Atassi, Z. Bagasharova Telmanovna, M. Saule, K. Kubanych, Microwave absorbing properties of ferrites and their composites: a review, *J. Magn. Magn. Mater.* 529 (2021), 167839, <https://doi.org/10.1016/j.jmmm.2021.167839>.
- [32] Y. Hou, X. Li, Q. Zhao, G. Chen, ZnFe₂O₄ multi-porous microbricks/graphene hybrid photocatalyst: facile synthesis, improved activity and photocatalytic mechanism, *Appl. Catal. B Environ.* 142–143 (2013) 80–88, <https://doi.org/10.1016/j.apcatb.2013.04.062>.
- [33] W. Shi, F. Guo, H. Wang, C. Liu, Y. Fu, S. Yuan, H. Huang, Y. Liu, Z. Kang, Carbon dots decorated magnetic ZnFe₂O₄ nanomaterials with enhanced adsorption capacity for the removal of dye from aqueous solution, *Appl. Surf. Sci.* 433 (2018) 790–797, <https://doi.org/10.1016/j.apsusc.2017.10.099>.
- [34] S.V.P. Vattikuti, A.K.R. Police, J. Shim, C. Byon, Sacrificial-template-free synthesis of core-shell C@Bi₂S₃ heterostructures for efficient supercapacitor and H₂ production applications, *Sci. Rep.* 8 (2018) 4194, <https://doi.org/10.1038/s41598-018-22622-0>.
- [35] W. Xu, J. Fang, Y. Chen, S. Lu, G. Zhou, X. Zhu, Z. Fang, Novel heterostructured Bi₂S₃/Bi₂Sn₂O₇ with highly visible light photocatalytic activity for the removal of rhodamine B, *Mater. Chem. Phys.* 154 (2015) 30–37, <https://doi.org/10.1016/j.matchemphys.2015.01.040>.
- [36] X.-J. Wen, C.-G. Niu, L. Zhang, G.-M. Zeng, Novel p-n heterojunction BiOI/CeO₂ photocatalyst for wider spectrum visible-light photocatalytic degradation of refractory pollutants, *Dalt. Trans.* 46 (2017) 4982–4993, <https://doi.org/10.1039/C7DT00106A>.

- [37] J. Deng, Y. Ge, C. Tan, H. Wang, Q. Li, S. Zhou, K. Zhang, Degradation of ciprofloxacin using α -MnO₂ activated peroxymonosulfate process: effect of water constituents, degradation intermediates and toxicity evaluation, *Chem. Eng. J.* 330 (2017) 1390–1400, <https://doi.org/10.1016/j.cej.2017.07.137>.
- [38] S. Giannakis, K.-Y.A. Lin, F. Ghanbari, A review of the recent advances on the treatment of industrial wastewaters by sulfate radical-based advanced oxidation processes (SR-AOPs), *Chem. Eng. J.* 406 (2021), 127083, <https://doi.org/10.1016/j.cej.2020.127083>.
- [39] D. Roy, S. Neogi, S. De, Visible light assisted activation of peroxymonosulfate by bimetallic MOF based heterojunction MIL-53(Fe/Co)/CeO₂ for atrazine degradation: pivotal roles of dual redox cycle for reactive species generation, *Chem. Eng. J.* 430 (2022), 133069, <https://doi.org/10.1016/j.cej.2021.133069>.
- [40] Y. Chen, X. Bai, Y. Ji, T. Shen, Reduced graphene oxide-supported hollow Co₃O₄@N-doped porous carbon as peroxymonosulfate activator for sulfamethoxazole degradation, *Chem. Eng. J.* 430 (2022), 132951, <https://doi.org/10.1016/j.cej.2021.132951>.
- [41] G. Wang, W. An, Y. Zhang, Z. Liu, S. Yang, P. Jin, D. Ding, Mesoporous carbon framework supported Cu-Fe oxides as efficient peroxymonosulfate catalyst for sustained water remediation, *Chem. Eng. J.* 430 (2022), 133060, <https://doi.org/10.1016/j.cej.2021.133060>.
- [42] J.-C.E. Yang, M.-P. Zhu, D.D. Dionysiou, B. Yuan, M.-L. Fu, Interplay of bicarbonate and the oxygen-containing groups of carbon nanotubes dominated the metal-free activation of peroxymonosulfate, *Chem. Eng. J.* 430 (2022), 133102, <https://doi.org/10.1016/j.cej.2021.133102>.
- [43] K. Wei, A. Armutlulu, Y. Wang, G. Yao, R. Xie, B. Lai, Visible-light-driven removal of atrazine by durable hollow core-shell TiO₂@LaFeO₃ heterojunction coupling with peroxymonosulfate via enhanced electron-transfer, *Appl. Catal. B Environ.* 303 (2022), 120889, <https://doi.org/10.1016/j.apcatb.2021.120889>.
- [44] D. Zhang, Y. Li, J. Guo, L. Zhou, Y. Lan, C. Chen, MOFs-derived magnetic C@Cu–Ni bimetal particles: an efficient peroxymonosulfate activator for 2,4,6-trichlorophenol degradation, *Chemosphere* 269 (2021), 129394, <https://doi.org/10.1016/j.chemosphere.2020.129394>.
- [45] D. Ma, J. Wu, M. Gao, Y. Xin, T. Ma, Y. Sun, Fabrication of Z-scheme g-C₃N₄/RGO/Bi₂WO₆ photocatalyst with enhanced visible-light photocatalytic activity, *Chem. Eng. J.* 290 (2016) 136–146, <https://doi.org/10.1016/j.cej.2016.01.031>.
- [46] G.V. Buxton, C.L. Greenstock, W.P. Helman, A.B. Ross, Critical Review of rate constants for reactions of hydrated electrons, hydrogen atoms and hydroxyl radicals (\cdot OH/ \cdot O $^-$ in Aqueous Solution, *J. Phys. Chem. Ref. Data* 17 (1988) 513–886, <https://doi.org/10.1063/1.555805>.
- [47] Y. Wang, F. Wu, Y. Mu, E.Y. Zeng, W. Meng, X. Zhao, J.P. Giesy, C. Feng, P. Wang, H. Liao, C. Chen, Directly predicting water quality criteria from physicochemical properties of transition metals, *Sci. Rep.* 6 (2016) 22515, <https://doi.org/10.1038/srep22515>.